Martinec and Velímský
Earth, Planets and Space (2022) 74:157
https://doi.org/10.1186/s40623-022-01716-0

Earth, Planets and Space

FULL PAPER

Open Access

An electric circuit model of the Earth's polar electrojets and field-aligned currents for the estimation of magnetospheric magnetic field from along-track Swarm magnetic data

Zdeněk Martinec[1,2*] and Jakub Velímský[2]

Abstract

This study deals with the analysis of Swarm vector magnetic data in order to create a circuit model of electric currents flowing in the Earth's polar ionosphere and the inner magnetosphere. The model is composed of a system of two-dimensional electric currents representing the magnetic fields of three-dimensional ionospheric polar electrojets (PEJs), the field-aligned currents (FACs), magnetospheric ring currents (MRCs) and magnetospherically induced electric currents inside the Earth (MICs) for each Swarm track. The aim of this paper is to model PEJ and FAC magnetic fields in terms of electric currents on a track-by-track base, subtract those magnetic fields from along-track Swarm magnetic data and estimate the magnetospheric magnetic field (MMF) in discrete time bins. The proposed method is primarily intended to apply to Swarm signals recorded during magnetic storms. The electric circuit model is set up in three steps. After subtracting the main, lithospheric, Sq ionospheric and oceanic tidal magnetic fields from along-track Swarm magnetic signals, the residuals are grouped in 1-h time bins and adjusted by the magnetic field of a two-circular loop model of MRCs and MICs represented by 3×2 parameters of the electric circular loops in the magnetosphere and the Earth. The adjustment is carried out for the X and Z magnetic field components only because the Y component contains a large signal due to FACs. In the second step, the modelled MRC–MIC magnetic field is removed from the original residuals and the reduced residuals are adjusted by the magnetic field of a system of two-dimensional electric circuits in the polar ionosphere and FACs. The circuit model is set up according to known geometry of PEJs and FACs. In the final step, the modelled magnetic fields of PEJs and FACs are subtracted from the original residuals and all three magnetic field components are adjusted by the MRC–MIC model, named MMC, in a similar way as in the first step. Reliability of the approach is demonstrated by the scatter plots of model MMC showing a significantly better agreement with Swarm magnetic field residuals than the existing MMFs.

Keywords: Ionosphere/magnetosphere interactions, Geomagnetic induction, Satellite magnetics

*Correspondence: zdenek@cp.dias.ie

[2] Department of Geophysics, Faculty of Mathematics and Physics, Charles University, V Holešovičkách 2, 180 00 Prague 8, Czech Republic
Full list of author information is available at the end of the article

Graphical Abstract

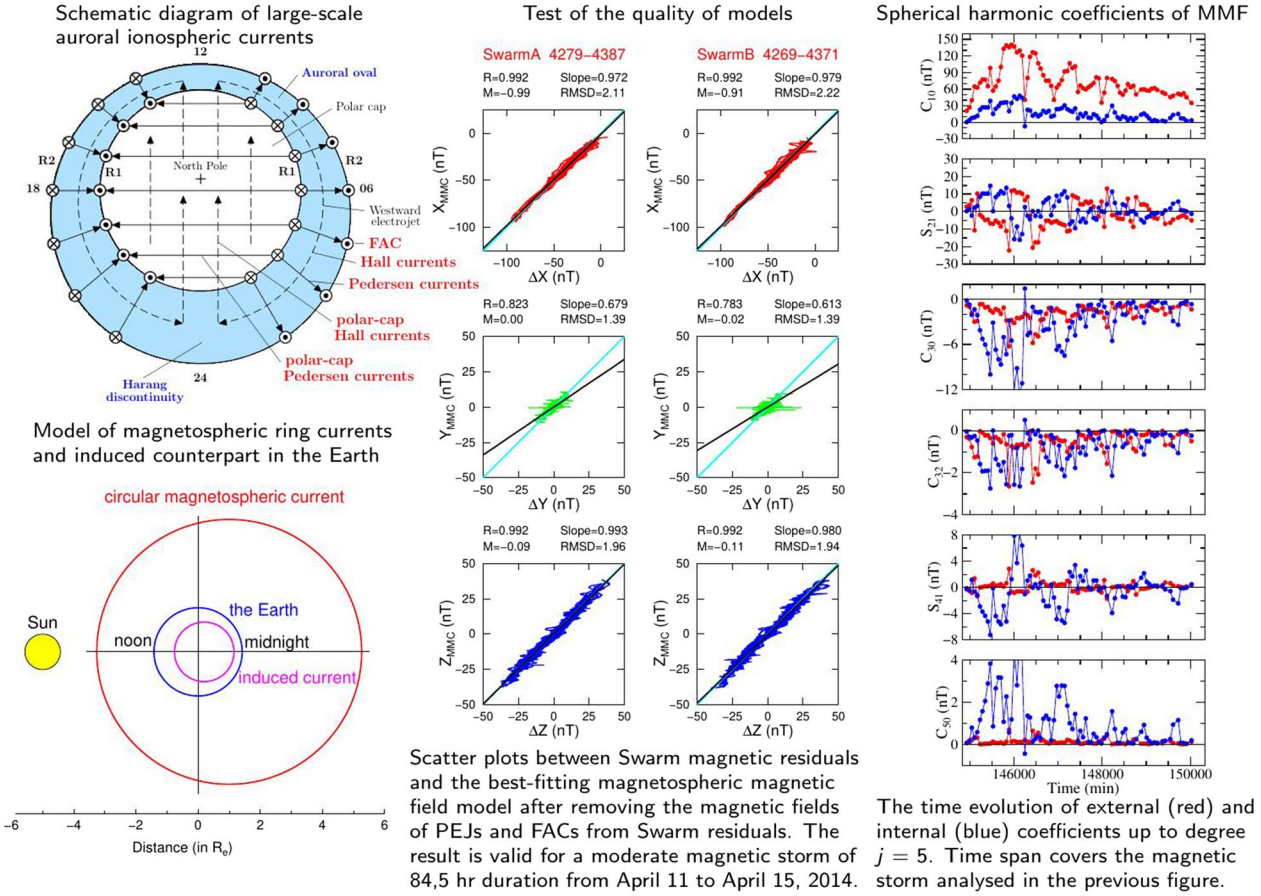

Scatter plots between Swarm magnetic residuals and the best-fitting magnetospheric magnetic field model after removing the magnetic fields of PEJs and FACs from Swarm residuals. The result is valid for a moderate magnetic storm of 84,5 hr duration from April 11 to April 15, 2014.

The time evolution of external (red) and internal (blue) coefficients up to degree $j = 5$. Time span covers the magnetic storm analysed in the previous figure.

Introduction

The extraction of the magnetospheric magnetic field (MMF) from along-track Swarm vector magnetic data and its separation into magnetospheric origin and its counterpart induced in the Earth is a demanding task when processing along-track Swarm vector magnetic data. There are, at least, two reasons which make data processing challenging.

First, degree-one spherical harmonics (SHs) of both the external (or primary, inducing) and internal (or secondary, induced) parts of MMF dominate the along-track Swarm magnetic residual signals (e.g., Shore et al. 2016), while the amplitudes of higher degree SHs of MMF decrease with increasing harmonic degree. If the ring current system in the inner magnetosphere consisting of a band of charged particles at geocentric distance R_m from 2 to 8 of the Earth's radius R_e would flow around concentric circles, the radial component of the primary and secondary MMFs at the Swarm satellite altitude of radius r were attenuated with increasing harmonic degree j as $(r/R_m)^{j-1}$ and $(R_e/r)^{j+2}$, respectively. However, the inner magnetosphere is, in fact, asymmetric, compressed by the solar wind dynamic pressure on the dayside, and stretched by the tail current on the nightside (e.g., Ganushkina et al. 2018). Thus, the magnetospheric ring currents are almost never symmetric rings. It implies that the amplitudes of higher degree SHs of MMF do not decrease exactly according to the above rule. For instance, the amplitudes of degree-two and degree-three SHs of the external part of MMF reach about 5% of the amplitude of degree-one SH at magnetically disturbed times (Martinec et al. 2018). As for the internal part of MMF, its degree-one SH is about one-third of the degree-one SH of the external part (Banks 1969). Higher degree SHs of the internal part of MMF decrease also with increasing spherical degree but, as indicated by the above rule, less rapidly than those of the external part. For instance, the amplitudes of degree-two or degree-three

SHs may reach 20% of the amplitude of degree-one SH at magnetically disturbed times (Martinec et al. 2018).

Second, Grayver et al. (2017) showed that the squared coherences between the external and internal degree-one SHs estimated from 3 years Swarm observations is larger than 0.98 for periods from 2 to 90 days. Likewise, Püthe et al. (2015) showed that the degree-one squared coherences over approximately the same interval of periods and for more than 10 years of magnetic satellite and observatory data exceed the value of 0.9. These values mean that 98% or 90% variability in the degree-one internal SH can be explained by the variability in degree-one external SH. The rest expresses noise or biases in data, the difficulty in detecting MMF signals in polar regions due to disturbing magnetic effect of ionospheric polar electrojets and field-aligned currents, but also the coupling between the external and internal magnetic field SHs of various degrees caused by lateral heterogeneities of the Earth's mantle electrical conductivity.

All it means that if the three-dimensional electrical conductivity structure of the Earth's mantle is to be recovered, which is one of the primary goals of the Swarm mission (Friis-Christensen et al. 2006), Swarm magnetic measurements need to be processed with maximum care such that higher degree SHs of MMF are estimated with high reliability. There are, at least, two approaches for estimating the MMF from Swarm measurements: the comprehensive inversion (e.g., Sabaka et al. 2020), followed by the non-comprehensive approach (Sabaka et al. 2018), and the two-step along-track spectral analysis by Martinec et al. (2018). Similarities and differences between those approaches are summarised by Martinec et al. (2018). Due to different processing schemes, the differences between the resulting models of MMF for degree-two and degree-three SHs are large.

Both data processing methods estimate MMF signals from mid-latitude Swarm data (Püthe et al. 2015; Martinec et al. 2018) and both assume that the magnetic effect of ionospheric polar electrojets (PEJs) and field-aligned currents (FACs) on mid-latitude Swarm data can be neglected. This may be a reason for the discrepancies in estimated higher degree SHs of MMF because PEJ and FAC magnetic signals that are present in mid-latitude measurements (actually, they are present in all Swarm measurements) propagate to the results of the two methods in a different way. Hence, one aim of this paper is to create an electric circuit model of PEJs and FACs and correct along-track Swarm magnetic measurements for the modelled PEJ and FAC magnetic fields.

The solar wind, magnetosphere and ionosphere are extremely spatio-temporal variable objects, where a large number of physical scenarios can develop and interconnect at the same time or sequentially. Although a remarkable progress has been made in quantitative analysis of the solar wind–magnetosphere–ionosphere system, it is hard to expect that a single universally accurate global model of this system will be created in near future. Further progress will, most likely, be to develop specialised or local models, e.g., valid in regional domains during magnetically disturbed times (Tsyganenko 2013). An example, developed in this paper, is a model of the magnetic fields of polar electrojets and field-aligned currents with a fine spatial resolution along satellite tracks of the low Earth orbit (LEO) satellite missions, such as CHAMP, Oersted, and Swarm.

A number of methods have been used to estimate the intensity and spatial distribution of ionospheric currents over the polar regions from ground magnetic data (Popov et al. 2001, and references therein). In fact, a ground magnetometer is mostly sensitive to the horizontal Hall currents while the ground magnetic perturbation due to the Pedersen current is almost exactly cancelled by the ground magnetic perturbation due to the field-aligned currents (Fukushima 1976; McHenry and Clauer 1987, and references therein). With the occurrence of satellite magnetic measurements, a model composed of a series of infinite line currents placed in the polar ionosphere has been applied to scalar satellite magnetic data to estimate the current density of the horizontal polar electrojets (Olsen 1996; Olsen et al. 2002; Moretto et al. 2002; Ritter et al. 2003; Aakjær et al. 2016). By vector satellite magnetic data, the FACs entering or leaving the high-latitude ionosphere can, in addition, be estimated. Juusola et al. (2006) used a 1D modification of the 2D Spherical Elementary Current System (SECS) method developed by Amm (1997) to estimate both the horizontal polar electrojets and FACs from CHAMP satellite vector magnetic data.

Both the line current method and 1D-SECS method assume that the FACs flow along radial lines of a uniform magnetic field between the ionosphere and the inner magnetosphere and, hence, FACs do not contribute to the magnetic field component parallel to the main magnetic field. This assumption is approximately valid in polar regions at quiet magnetic times, but it is rather violated at magnetically disturbed times when the earthward edge of the inner magnetosphere moves closer to the ionosphere up to geocentric distances of $\sim 3R_e$ (e.g., Baumjohann and Treumann 1996; Daglis et al. 1999; Tsyganenko 2013; Chen 2020) and the curvature of field lines of the main magnetic field becomes important (see "Estimation of the auroral oval locations" section). In this paper, we will abandon the assumption of a uniform main magnetic field and consider FACs flowing along the field lines of the Earth's magnetic dipole, which is a more

realistic FAC geometry valid up to geocentric distances of $\sim 8R_e$ (e.g., Daglis et al. 1999; Tsyganenko 2013).

The circuit model used to analyse of Swarm vector magnetic data in this paper is composed of a system of two-dimensional (2D) electric currents that represent the magnetic fields of three-dimensional (3D) ionospheric polar electrojets and field-aligned currents. Prokhorov et al. (2018) considered a 3D distribution of the ionospheric current density with latitudinal and vertical structures. They compare magnetic field calculation using 2D (so-called equivalent currents) and 3D current distribution. They showed that the 2D approximation of the ionospheric current system improves significantly the computation performance in comparison with the method based on a 3D current system. Therefore, they recommend to use 2D currents as a fast and relatively accurate solution for magnetic field calculation.

The aim of this paper is to extract the magnetic signals of magnetospheric ring currents and their counterparts induced in the Earth from Swarm satellite vector magnetic data grouped in discrete time bins. The paper first presents a description of the data selection procedure followed by the definition of the magnetic residuals used as the input data for the modelling performed in this paper. The following section presents the model of two electric circular loops placed in the inner magnetosphere and inside the Earth that is used to adjust the magnetic field of magnetospheric ring currents (MRCs) and the magnetospherically induced currents (MICs) inside the Earth. Then, the description of the topology of large-scale current systems in the polar ionosphere are shortly summarised followed by the approach of estimating the auroral oval locations. After finding the location of the auroral ovals and subtracting the modelled MRC–MIC magnetic field from the input residuals, the modified residuals are adjusted by the magnetic field of a model composed of 2D electric circuits placed in the auroral ovals and the magnetic field of the currents flowing along the field lines of the Earth's magnetic dipole connecting the polar ionosphere and magnetosphere. The adjustment is carried out over a complete Swarm track, that is, over mid-latitudes and both polar regions. Important is that the residuals to be adjusted by PEJ and FAC magnetic fields are reduced for the magnetospheric magnetic field estimated in the first step, so the PEJ–FAC model does not capture the field due to MRCs and MICs. In the final step, the magnetic field of the best-fitting PEJ–FAC electric circuit model is subtracted from the input residuals and the modified residuals are adjusted again by a two-circular loop model of MRCs and MICs, similar to that employed in the first step. The quality of the new MMF model, named model MMC, is assessed by the scatter plots between residuals and modelled fields, and compared with the scatter plots of existing MMA (Sabaka et al. 2020) and MME (Martinec et al. 2018) models of MMF.

Data selection

To extract the magnetic signals of MRCs and MICs from the along-track satellite vector magnetic measurements made by Swarm satellites, we use the magnetic field vector data sets (with 1 s resolution) of the Level-1B products of the Swarm mission (Olsen et al. 2013). In addition to time and position, the data file contains the magnetic scalar intensity and the three components of the magnetic vector in the North–East–Center (NEC) local Cartesian coordinate frame. The present study is based on version 0601 of Swarm Level-1b NEC product.

In the first step, the geomagnetic main field and the lithospheric magnetic field, as given by the CHAOS-7.9 field model (Finlay et al. 2020), denoted as $\boldsymbol{B}_{\rm CHAOS}$, the ionospheric Sq and oceanic M_2 tidal magnetic fields, as given by the models MIO_SHA_2C_0701 and MTI_SHA_2C_0701 (Sabaka et al. 2020), denoted as $\boldsymbol{B}_{\rm MIO}$ and $\boldsymbol{B}_{\rm MTI}$, respectively, are calculated for Swarm satellite positions and subtracted from the vector magnetic measurements $\boldsymbol{B}_{\rm Swarm}$ with a time step of 1 s. The resulting residual magnetic field

$$\Delta\boldsymbol{B} = \boldsymbol{B}_{\rm Swarm} - \boldsymbol{B}_{\rm CHAOS} - \boldsymbol{B}_{\rm MIO} - \boldsymbol{B}_{\rm MTI} \tag{1}$$

can be represented in terms of spherical components $\Delta X, \Delta Y$ and ΔZ as

$$\begin{aligned}\Delta\boldsymbol{B}(r,\Omega,t) = &-\Delta Z(r,\Omega,t)\boldsymbol{e}_r - \Delta X(r,\Omega,t)\boldsymbol{e}_\vartheta \\ &+ \Delta Y(r,\Omega,t)\boldsymbol{e}_\varphi,\end{aligned} \tag{2}$$

where r and Ω are the geocentric spherical coordinates of the satellite's location, Ω stands for the colatitude ϑ and longitude φ pair, t is time, and $\boldsymbol{e}_r$, $\boldsymbol{e}_\vartheta$ and $\boldsymbol{e}_\varphi$ are the spherical unit base vectors. Despite the magnetic field of ionospheric Sq currents being removed from residuals $\Delta\boldsymbol{B}$, we will use only nightside data in this study. We should emphasise that the residual magnetic field $\Delta\boldsymbol{B}$ is the input data for the modelling carried out in this paper.

We will compare the results of two approaches for estimating MMF from Swarm vector magnetic data: the comprehensive inversion (e.g., Sabaka et al. 2020), followed by the non-comprehensive approach (Sabaka et al. 2018), and the two-step along-track spectral analysis by Martinec et al. (2018). The time series resulting from the comprehensive inversion are provided as a Swarm mission Level 2 product by the European Space Agency. We will refer to the current version of this data model and the model of MMF estimated by the two-step along-track spectral analysis as model MMA_SHA_2C_0604 (shortly, model MMA) and model MME model, respectively. A possible way to compare the results of the two methods

is to calculate the coherences between models MMA and MME. Ideally, the coherence should equal to 1, which is the case where the two methods give the same results for the same input data. Martinec et al. (2018) showed that only degree-one SHs, both external and internal, approach this case, while degree-two and degree-three SHs are out of coherence. The question arises as to what is the reason.

Another way to assess a model's quality is to calculate the correlation coefficient between the observed and model field components. As an example, Fig. 1 shows the scatter plots and the linear fits between the Swarm magnetic residuals ΔX, ΔY and ΔZ and the components of the MMA model of the magnetospheric magnetic field along Swarm satellite tracks for a moderate magnetic storm of 84,5-h duration. The plots correspond to the Swarm satellite positions with colatitudes ϑ's from the mid-latitude interval $I^{10^\circ}_{\rm ML}$, $\vartheta \in I^{10^\circ}_{\rm ML}$, where $I^{10^\circ}_{\rm ML} = (\vartheta_{\rm R^n_2} + 10^\circ, \vartheta_{\rm R^s_2} - 10^\circ)$, and $\vartheta_{\rm R^n_2}$ and $\vartheta_{\rm R^s_2}$ are colatitudes of equatorward Region 2 of the northern and southern auroral ovals, respectively. Their values are estimated further in "Estimation of the auroral oval locations" section. Here, all Swarm positions near, or in, polar regions, that is, for $\vartheta < \vartheta_{\rm R^n_2} + 10^\circ$ and $\vartheta > \vartheta_{\rm R^s_2} - 10^\circ$ are excluded from the comparison due to the overwhelming dominance of PEJs and FACs. The choice of mid-latitude interval reflects a trade-off between minimising the effect of PEJs and FACs on mid-latitude residuals and maximising the reliability of degree-one and higher degree SH estimates, as discussed in "Electric two-circular loop model of MRCs and MICs" section. For example, making the mid-latitude interval shorter, the disturbing effect of PEJs and FACs will be reduced but the estimate of higher degree SHs of MMF will decrease in reliability.

Figure 1 shows that the correlation between the residual Swarm signals and the MMA signals is largest for the Z component ($R \approx 0.96$, an average for three Swarm satellites), smaller for the X component ($R \approx 0.85$) and least for the Y component ($R \approx 0.81$). A slope of least-squares regression line for the Z, X and Y components has respective values $S \approx 0.84$, 0.77 and 0.49. The spread of data, measured in terms of the root mean squares of the differences between the MMA values and the predicted values from the regression line (RMSD) is smallest for the Z component (RMSD ≈ 4.1 nT) and largest for the X component (RMSD ≈ 8.3 nT). A large value of mean M for the X component ($M \approx -13.4$ nT) indicates that there is a systematic bias in the X component of MMA model. Since PEJ and FAC magnetic effects are not considered in processing of Swarm data by the comprehensive approach (Sabaka et al. 2020), the single measures of central tendency between data and model in Fig. 1 (that is, R, S, M and RMSD) indicate that PEJs and FACs mainly disturb the X and Y components, but less seriously the Z component of Swarm magnetic measurements. In addition, we can observe that the scatter plots for Swarm A and Swarm C tracks are similar, indicating a scatter plot is invariant to small change in satellite track position.

Similar to Figs. 1, 2 shows the scatter plots for the components of model MME (Martinec et al. 2018). Comparing Figs. 1 and 2, we can see that model MME performs similarly to model MMA in the Z component ($R \approx 0.97$, $S \approx 1.06$), significantly better in the X component ($R \approx 0.97$, $S \approx 0.91$), and worse in the Y component ($R \approx 0.25$, $S \approx 0.10$) than model MMA. The differences between these figures can be attributed to different ways of processing Swarm magnetic data (Martinec et al. 2018) such that the magnetic fields of PEJs and FACs contaminating the mid-latitude Swarm data propagate into the resulting estimates of MMF differently. In particular, a large spread of the azimuthal Y component of model MME can be explained by the way of how the two-step along-track spectral method by Martinec et al. (2018) processes the data; it adjusts along-track Swarm residuals ΔX and ΔZ, but not ΔY. A less scatter of the Y component of model MMA may be explained by the assumption made by the non-comprehensive approach (Sabaka et al. 2018) that MMF in time bins of 1.5 h (for the estimation of degree-one SHs) and 6 h (for higher degree SHs) duration are static such that more than one satellite track data can be analysed within a discrete time bin; then, a certain azimuthal dependency of MMF may be revealed. However, a 'static' assumption is questionable at magnetically disturbed times. We will return to this point in "A revised estimate of MMF" section.

Electric two-circular loop model of MRCs and MICs

As Figs. 1 and 2 indicate, a way to improve the quality of MMF models is to take into account the magnetic effect of PEJs and FACs when processing mid-latitude Swarm magnetic data. In fact, both MRCs and MICs, and PEJs and FACs contribute to the long-wavelength part of mid-latitude magnetic residuals ΔX, ΔY and ΔZ, but each of them in a different way. The long-wavelength part of ΔZ mainly originates in the large-scale MRCs and MICs, while the long-wavelength part of ΔX is mainly due to both MRCs and MICs, and PEJs. As far the long-wavelength part of mid-latitude ΔY, it is mainly due to PEJs and FACs. All these contributions may reach hundreds of nT during magnetic storms. On the other hand, the contribution due to PEJs and FACs to mid-latitude residual ΔZ is rather weak and often neglected when extracting the MMF from mid-latitude Swarm data (Sabaka et al. 2020; Martinec et al. 2018). At the same time, however, the contribution due to PEJs and FACs to mid-latitude

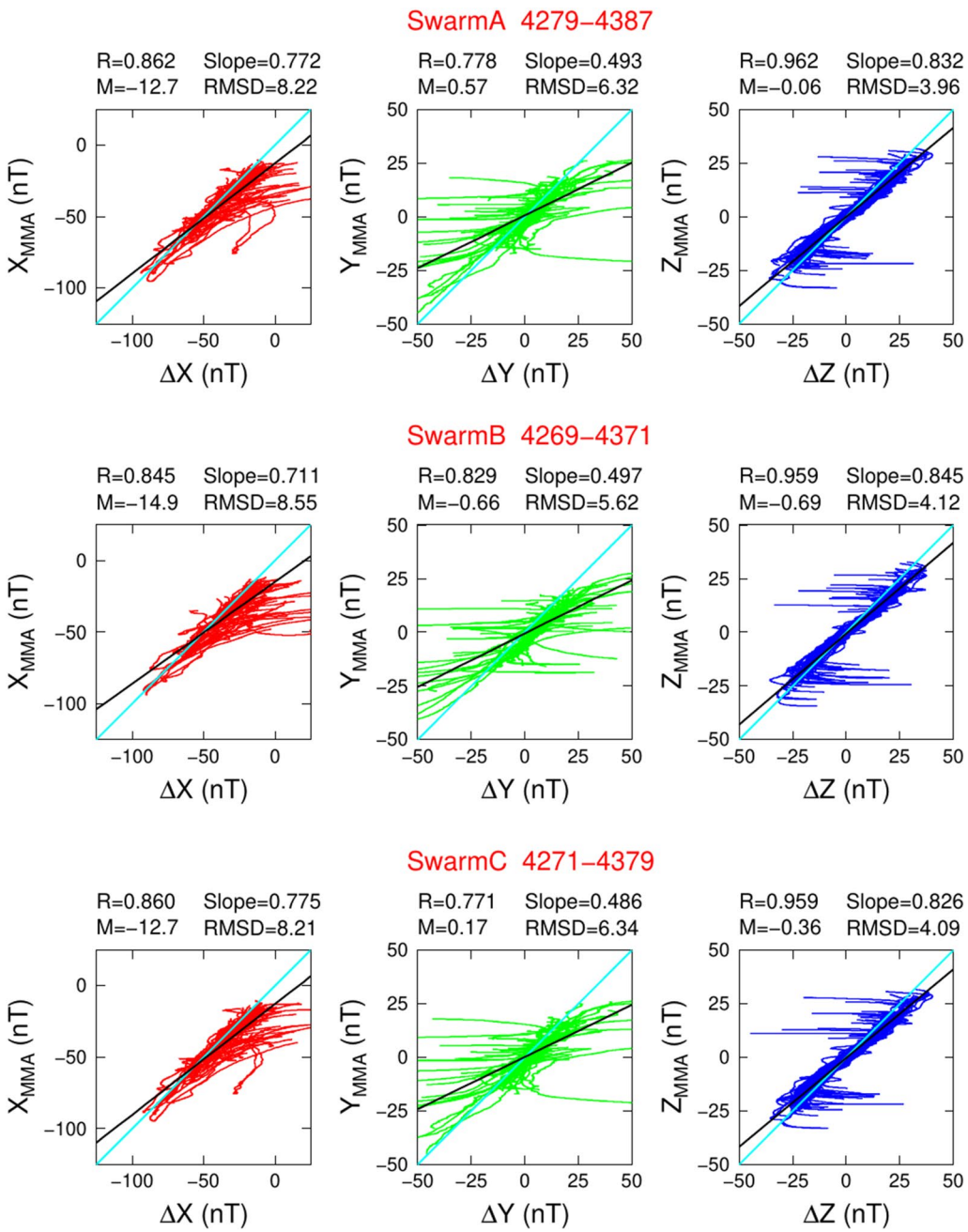

Fig. 1 The scatter plots and linear fits between the Swarm magnetic residuals ΔX (red), ΔY (green) and ΔZ (blue) and the components X_{MMA}, Y_{MMA} and Z_{MMA} of the MMA model of the magnetospheric magnetic field (Sabaka et al. 2020) along Swarm A (top panels), Swarm B (middle panels) and Swarm C (bottom panels) satellite tracks. The results are shown for a moderate magnetic storm of 84,5-h duration from April 11 to April 15, 2014. The Dst index equals −81at the main phase of the storm. Swarm satellite track numbers are given in the headers of panels. Only data from the mid-latitude interval $I_{\mathrm{ML}}^{10^\circ}, I_{\mathrm{ML}}^{10^\circ} = (\vartheta_{\mathrm{R}_2^{\mathrm{n}}} + 10^\circ, \vartheta_{\mathrm{R}_2^{\mathrm{s}}} - 10^\circ)$, are included. A least-squares regression line is shown by black line. The corresponding correlation coefficient (R), regression slope (S) and mean (M in nT) are shown in each panel. In addition, RMSD (in nT) shows the root mean squares of the differences between the MMA and the predicted values from the regression line. For comparison, light-blue line stands for the exact linear relationship between Swarm residuals and a modelled field

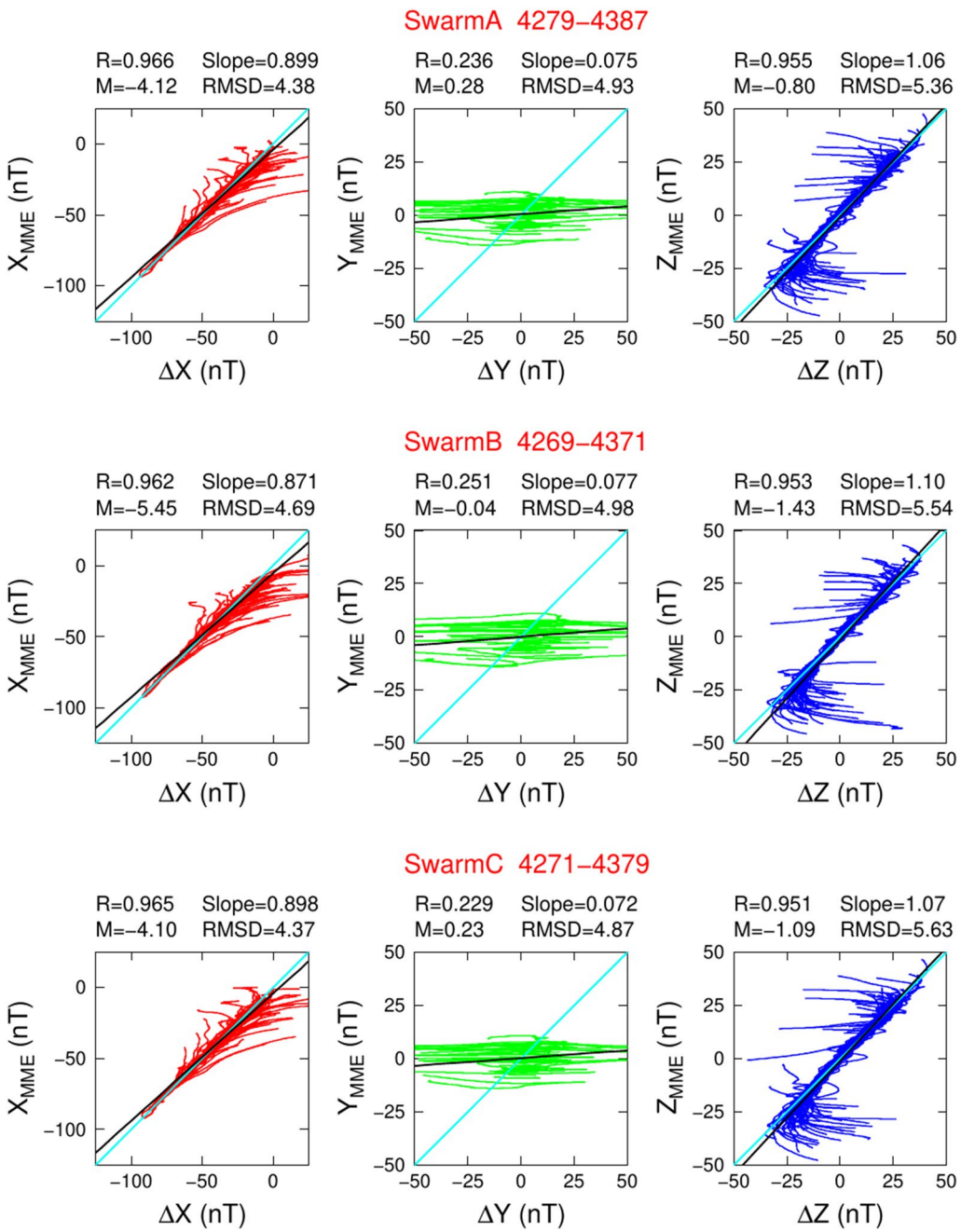

Fig. 2 The same as Fig. 1, but for model MME. The cut-off degree of the along-track spectral analysis is equal to 3 (Martinec et al. 2018)

residual ΔX is also neglected, which is a rather rough approximation, as discussed below.

In addition, the spatial patterns of the mid-latitude magnetic fields due to MRCs and MICs, and due to PEJs and FACs are different. The Z magnetic field component due to MRCs and MICs changes with colatitude ϑ predominantly as the cosine of colatitude, that is, as the Legendre function $P_{10}(\cos\vartheta)$, while the X component changes as the sine of colatitude, that is, as the derivative of $P_{10}(\cos\vartheta)$ with respect to ϑ (Banks 1969; Shore et al. 2016). Hence, degree-one SH of the X component of MMF reaches maximum at the magnetic equator. As far the magnetic fields of PEJs and FACs, they monotonically decrease with increasing distance from the polar regions because the magnetic field decreases as the distance from the source increases. Hence, the magnetic fields of PEJs

and FACs reach their minima near the magnetic equator depending on the spatial distribution of PEJs and FACs in polar regions. The different mid-latitude spatial patterns of the X component due to MRCs and MICs, and PEJs and FACs help to separate them in terms of degree-one SHs.

The situation with higher degree SHs is different. The X component of MMF for degree-two SHs changes with colatitude ϑ as function $\sin\vartheta\cos\vartheta$, which reaches two extrema near the polar regions at $\vartheta = 45°$ and $135°$. Hence, the degree-two magnetic field in mid-latitudes can be overlapped by a stronger magnetic field of PEJs (and slightly by FACs) at magnetically disturbed times. Similarly, the degree-three SH of the X component of MMF reaches three extrema, one at the equator and the other two near the polar regions at $\vartheta \sim 30°$ and $\sim 150°$. Hence, this magnetic field can again be easily overlapped by PEJ and FAC magnetic fields. In summary, the SH analysis of along-track residuals ΔX and ΔZ provides a good-quality estimate of degree-one SH of MMF, while the quality of degree-two or degree-three SHs is questionable due to the overlap of MMF signals by PEJ and FAC magnetic fields at magnetically disturbed times.

In view of these arguments, to estimate higher degree SHs of MMF with a good confidence, the use of SH analysis of the Swarm magnetic residuals is problematic. Instead, we will create a complex electric circuit model of the currents flowing in the polar ionosphere, the inner magnetosphere and along the field lines connecting the two domains, and will determine the magnetic field due to the electric circuit model along Swarm tracks. The model consists of 2D electric circuits that are set up according to a simplified geometry of the currents flowing in and between the two regions.

As the magnetospheric ring currents in the inner magnetosphere, PEJs and FACs are strongly related to the Earth's magnetic field, we will use the spherical solar magnetic coordinates (SM) $r, \vartheta_{\rm sm}, \varphi_{\rm sm}$ (Laundal and Richmond 2017) rather than spherical geographic coordinates r, ϑ, φ. We transform spherical magnetic field residuals ΔX, ΔY and ΔZ in geographic coordinates to spherical magnetic field residuals $\Delta X_{\rm sm}$, $\Delta Y_{\rm sm}$ and ΔZ in SM coordinates, and use the latter. Swarm vector magnetic residual field (2) transformed to SM coordinates takes the form

$$\begin{aligned}\Delta\boldsymbol{B}_{\rm sm}(r,\Omega_{\rm sm},t) = &-\Delta Z(r,\Omega_{\rm sm},t)\boldsymbol{e}_r\\ &-\Delta X_{\rm sm}(r,\Omega_{\rm sm},t)\boldsymbol{e}_{\vartheta_{\rm sm}}\\ &+\Delta Y_{\rm sm}(r,\Omega_{\rm sm},t)\boldsymbol{e}_{\varphi_{\rm sm}},\end{aligned} \tag{3}$$

where $\Omega_{\rm sm} = (\vartheta_{\rm sm}, \varphi_{\rm sm})$, and $\boldsymbol{e}_{\vartheta_{\rm sm}}$ and $\boldsymbol{e}_{\varphi_{\rm sm}}$ are the horizontal spherical unit base vectors in the SM coordinates. Note that residual ΔZ does not change by the rotation from the geographic to SM coordinates because the radial spherical base vector $\boldsymbol{e}_r$ does not change by this rotation.

Let us start with creating an electric circuit model of MRCs and MICs. The circuit model in SM coordinates consists of two electric circular loops lying on the dipole equatorial plane (i.e., the $x_{\rm sm}y_{\rm sm}$ plane) and are shifted along the $x_{\rm sm}$ axis, see Fig. 3. The circles are described by the parametric equations (C.1). The magnetic field generated by a steady electric current flowing along a circular loop is given by the line integral (A.3) of infinitesimal magnetic field contributions expressed by the Biot–Savart law (B.9). The line integral is calculated by a numerical quadrature over the full planar angle.

The two-circular loop model is represented by 6 parameters, that is, radii a_e and a_i of the external and internal circles, shifts x_{0e} and x_{0i} of the circles along the $x_{\rm sm}$ axis and steady electric currents I_e and I_i flowing along the circles. The model is designed such that residuals $\Delta X_{\rm sm}$ and ΔZ of three Swarm satellites are grouped in discrete bins of 1 hour duration, similar to Sabaka et al. (2020), and the multi-track residuals over mid-latitudes are optimally adjusted by the magnetic field of MRC–MIC model.

It is important to emphasise that the duration of bins can be further increased at magnetically quiet times. For example, Sabaka et al. (2018)'s non-comprehensive approach uses the bins of 1.5-h and 6-h duration for estimating degree-one and higher degree SHs of MMF, respectively. However, at magnetically disturbed times when PEJs, FACs and MMFs are quickly changing in time and space, the increase of bin duration may result

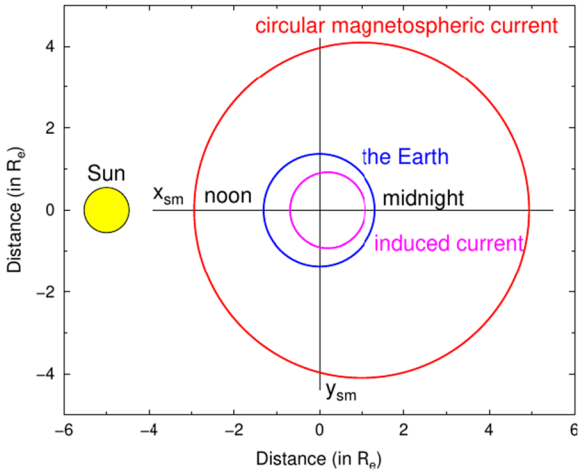

Fig. 3 Circular model of a magnetospheric ring current and its counterpart induced in the Earth. The scale does not match the reality

in larger differences between the residuals and modelled MMF. To avoid this feature, it would be necessary to group the residuals in non-uniform time bins with a longer duration at magnetically quiet times and a shorter duration at magnetically disturbed times. A non-uniform time binning can be done, for instance, according to the proxy RC index (Onovughe 2018; Sabaka et al. 2020), which will be treated in a separate publication. Note, at least, that a non-uniform time binning does not make a significant complication, for example, in modelling of electromagnetic induction (EMI) in the Earth's mantle provided that the forward EMI modelling is carried out in the time domain (Martinec et al. 2003; Velímský and Martinec 2005).

Note that residuals $\Delta Y_{\rm sm}$ are not included in the adjustment because they contain a large magnetic signal due to FACs during magnetically disturbed times. After modelling magnetic field of FACs, this field will be removed from $\Delta Y_{\rm sm}$ and an enhanced estimate of MMF will be carried out in "A revised estimate of MMF" section.

The adjustment of the Swarm residuals $\Delta X_{\rm sm}$ and ΔZ is non-linear with respect to geometric parameters a_e, x_{0e}, a_i, x_{0i} and linear with respect to current amplitudes I_e and I_i. The non-linear geometric parameters are found by a grid search over a specified range of parameters, while the amplitudes of electric currents are estimated by least squares.

The non-linear adjustment for estimating parameters a_e, x_{0e}, a_i, x_{0i} is, however, non-unique. That is, a large number of parameter combinations can adjust along-track Swarm residuals within the accuracy of the data. Since many of these combinations are physically unacceptable, we limit the range of parameter variability as follows:

$$\begin{aligned} 4 \le a_e/R_e &\le 8, \\ 0.4 \le a_i/R_e &\le 0.7, \\ -2 \le x_{0e}/R_e &\le 2, \\ -0.2 \le x_{0i}/R_e &\le 0.2. \end{aligned} \tag{4}$$

The interval of a_e approximates the interval of geocentric distances where the ring currents in the inner magnetosphere encircles the Earth (e.g., Daglis et al. 1999; Tsyganenko 2013), while the interval for x_{0e} reflects a non-uniformity of the ring currents; magnetosphere is essentially asymmetric, compressed by the solar wind dynamic pressure on the dayside, and stretched by the tail current on the nightside (e.g., Ganushkina et al. 2018). The electric currents induced in the Earth by the MRCs are limited to flow within the geocentric distance intervals for a_i and x_{0i}.

We should emphasise that the six-parameter circuit model of two shifted circles lying on the dipole equatorial plane in the magnetosphere and the Earth significantly simplifies the currents flowing in the inner magnetosphere and the Earth at magnetically disturbed times. It would be possible to adopt more complex circuit models of these currents, e.g., more-than-two shifted circles. However, as Fig. 4 shows for six selected Swarm A tracks (see Table 1), the two-circle model adjusts mid-latitude residuals $\Delta X_{\rm sm}$ and ΔZ solidly well. The differences between the Swarm residuals and the best-fitting signals usually do not exceed ±5 nT at magnetically disturbed times. Making a circuit model more complex, the

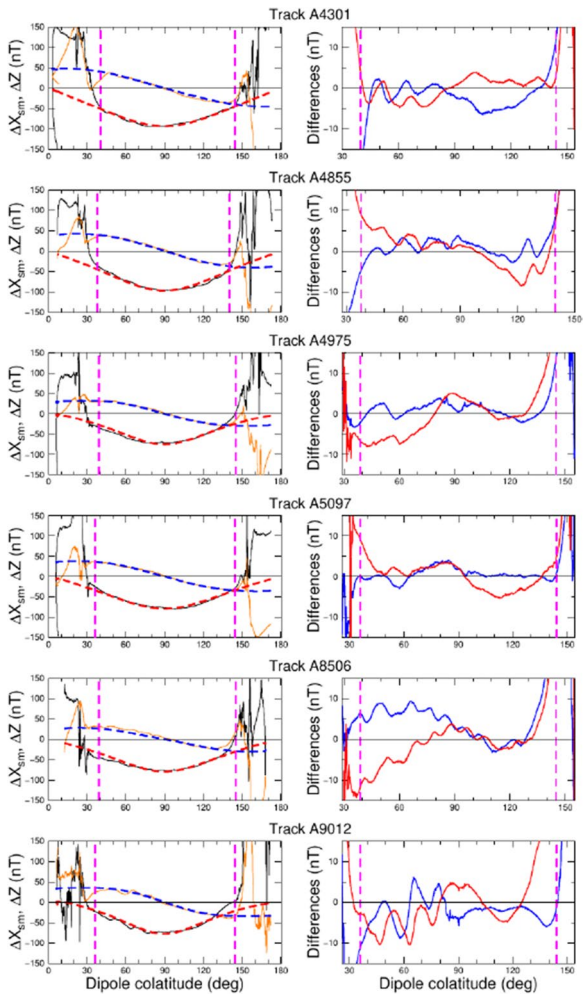

Fig. 4 Left panels: The Swarm residuals $\Delta X_{\rm sm}$ (thin black) and ΔZ (thin orange) along six Swarm A nightside full tracks (see Table 1) and best-fitting signals $X^{(1)}_{\rm sm,MMC}$ (dashed red) and $Z^{(1)}_{\rm MMC}$ (dashed blue) over the mid-latitude interval $I^{10^\circ}_{\rm ML}$ (vertical dashed violet lines) due the two-circular loop model of MRCs and MICs. Right panels: The differences $\Delta X_{\rm sm} - X^{(1)}_{\rm sm,MMC}$ (red) and $\Delta Z - Z^{(1)}_{\rm MMC}$ (blue) over mid-latitude interval $I^{10^\circ}_{\rm ML}$. Here, $I^{10^\circ}_{\rm ML} = (\vartheta_{{\rm sm},R^{\rm n}_2} + 10^\circ, \vartheta_{{\rm sm},R^{\rm s}_2} - 10^\circ)$, and $\vartheta_{{\rm sm},R^{\rm n}_2}$ and $\vartheta_{{\rm sm},R^{\rm s}_2}$ are dipole colatitudes of equatorward Region 2 of the northern and southern auroral ovals, respectively

Table 1 Swarm A satellite tracks selected to demonstrate the results for moderately disturbed times

Track no.	Date	UTC	LT	Dst	Kp
A4301	12.04.2014	08.42	02.04	− 86	4^+
A4855	30.04.2014	10.72	00.42	− 65	3
A4975	04.05.2014	08.68	00.06	− 47	4
A5097	08.05.2014	08.23	23.72	− 39	3^+
A8506	27.08.2014	13.03	01.74	− 58	4
A9012	13.09.2014	01.05	00.26	− 63	6^+

The coordinated universal time (UTC) and the local time (LT) are the respective times when Swarm A satellite passes the magnetic equator

adjustment for estimating the model parameters would suffer from even more severe non-uniqueness than the applied six-parameter model.

Let the components of the magnetic field generated by the two-circular loop model of MRCs and MICs best fitting the mid-latitude residuals $\Delta X_{\rm sm}$ and ΔZ be denoted as $X^{(1)}_{\rm sm,MMC}$ and $Z^{(1)}_{\rm MMC}$. The component $Y^{(1)}_{\rm sm,MMC}$ is computed a posteriori for the parameters of the best-fitting two-circles model. Label '(1)' indicates that $X^{(1)}_{\rm sm,MMC}$, $Y^{(1)}_{\rm sm,MMC}$ and $Z^{(1)}_{\rm MMC}$ are the first-order estimates of MMF in the sense that no corrections due to PEJs and FACs have been applied. Furthermore, label 'C' in 'MMC' indicates that the MMF is modelled by electric current systems rather than by a SH model such as model MMA (Sabaka et al. 2020) or model MME (Martinec et al. 2018).

Figure 5 shows the scatter plots between the Swarm magnetic residuals $\Delta X_{\rm sm}$, $\Delta Y_{\rm sm}$ and ΔZ and the best-fitting magnetospheric magnetic fields $X^{(1)}_{\rm sm,MMC}$, $Y^{(1)}_{\rm sm,MMC}$ and $Z^{(1)}_{\rm MMC}$ for the same moderate magnetic storm as analysed in Figs. 1 and 2. Comparing these figures, we can see that the single measures of the quality of fit, that is, R, S, M and RMSD, are a bit more favourable for the Z component of model MMC$^{(1)}$ than that of model MME. The same holds for the X component except for RMSD that is larger by about 1-3 nT for model MMC$^{(1)}$, but smaller by about 3 nT than that of model MMA. Though the Y component of model MMC$^{(1)}$ has been calculated a posteriori from the parameters of the model best-fitting $\Delta X_{\rm sm}$ and ΔZ, the scatter plots of the Y component, shown in the middle panels of Fig. 5, have practically zero slope and insignificant correlation between residuals $\Delta Y_{\rm sm}$ and model field component $Y^{(1)}_{\rm sm,MMC}$ because the two-circular loop model adjusts only residuals $\Delta X_{\rm sm}$ and ΔZ, but not $\Delta Y_{\rm sm}$ (similarly as model MME). The adjustment of all three residuals will be done in "A revised estimate of MMF" section. At this moment, we may assume that $\Delta Y_{\rm sm}$ is predominantly generated by PEJs and FACs.

A new residual magnetic field $\Delta \boldsymbol{B}^{(1)}_{\rm sm}$ can be defined by subtracting the best-fitting magnetospheric magnetic field $\boldsymbol{B}^{(1)}_{\rm sm,MMF}$, that is, the field

$$\begin{aligned}\boldsymbol{B}^{(1)}_{\rm sm,MMC}(r,\Omega_{\rm sm},t) = &- Z^{(1)}_{\rm MMC}(r,\Omega_{\rm sm},t)\boldsymbol{e}_r \\ &- X^{(1)}_{\rm sm,MMC}(r,\Omega_{\rm sm},t)\boldsymbol{e}_{\vartheta_{\rm sm}} \\ &+ Y^{(1)}_{\rm sm,MMC}(r,\Omega_{\rm sm},t)\boldsymbol{e}_{\varphi_{\rm sm}},\end{aligned} \tag{5}$$

from the Swarm residuals $\Delta \boldsymbol{B}_{\rm sm}$, given by Eq. (3), as

$$\Delta \boldsymbol{B}^{(1)}_{\rm sm} = \Delta \boldsymbol{B}_{\rm sm} - \boldsymbol{B}^{(1)}_{\rm sm,MMC}. \tag{6}$$

A schematic topology of large-scale current systems in the polar ionosphere

There is an extensive literature dealing with the physical processes in the Earth's magnetosphere and ionosphere, their observations by the ground-based magnetic observatories and satellites, and the interaction between the magnetosphere and ionosphere (e.g., Kamide 1982; Milan et al. 2017; Ganushkina et al. 2018). Here, we present only a schematic view on the topology of large-scale current systems in the polar ionosphere in order to be able to compile an approximate geometric model of those currents.

The auroral ovals (or zones) are regions in the high-latitude ionosphere where the ionisation of neutral atoms and molecules by the precipitation of magnetospheric energetic electrons and ions enhances the electrical conductivity. The auroral zones are approximately a bell whose centre is displaced about five degrees along the midnight meridian from the geomagnetic pole (e.g., Baumjohann and Treumann 1996). Since the conductivity of the auroral zone is much higher than the conductivity of the polar cap, the high-latitude currents are concentrated inside the auroral zones, where they form large-scale electric horizontal currents, named the auroral electrojets. Two strong auroral electrojets can be seen near to 70° latitude (e.g., Johnsen 2013; Liou et al. 2018). The dimensions of the polar cap and auroral oval are subject to strong temporal variations. Whereas both regions contract to a relatively narrow region around the magnetic pole during magnetically quiet conditions, the diameter of the polar cap and width of the auroral oval both expand during magnetically active conditions.

The magnetosphere and ionosphere are electromagnetically coupled through the field-aligned currents. By definition, the field-aligned currents (FACs) flow along the Earth's magnetic field lines represented, in this paper, by the dipole field lines. As shown in Fig. 6, the paired downward and upward FACs connect the magnetosphere with the high-latitude ionosphere via two regions, named

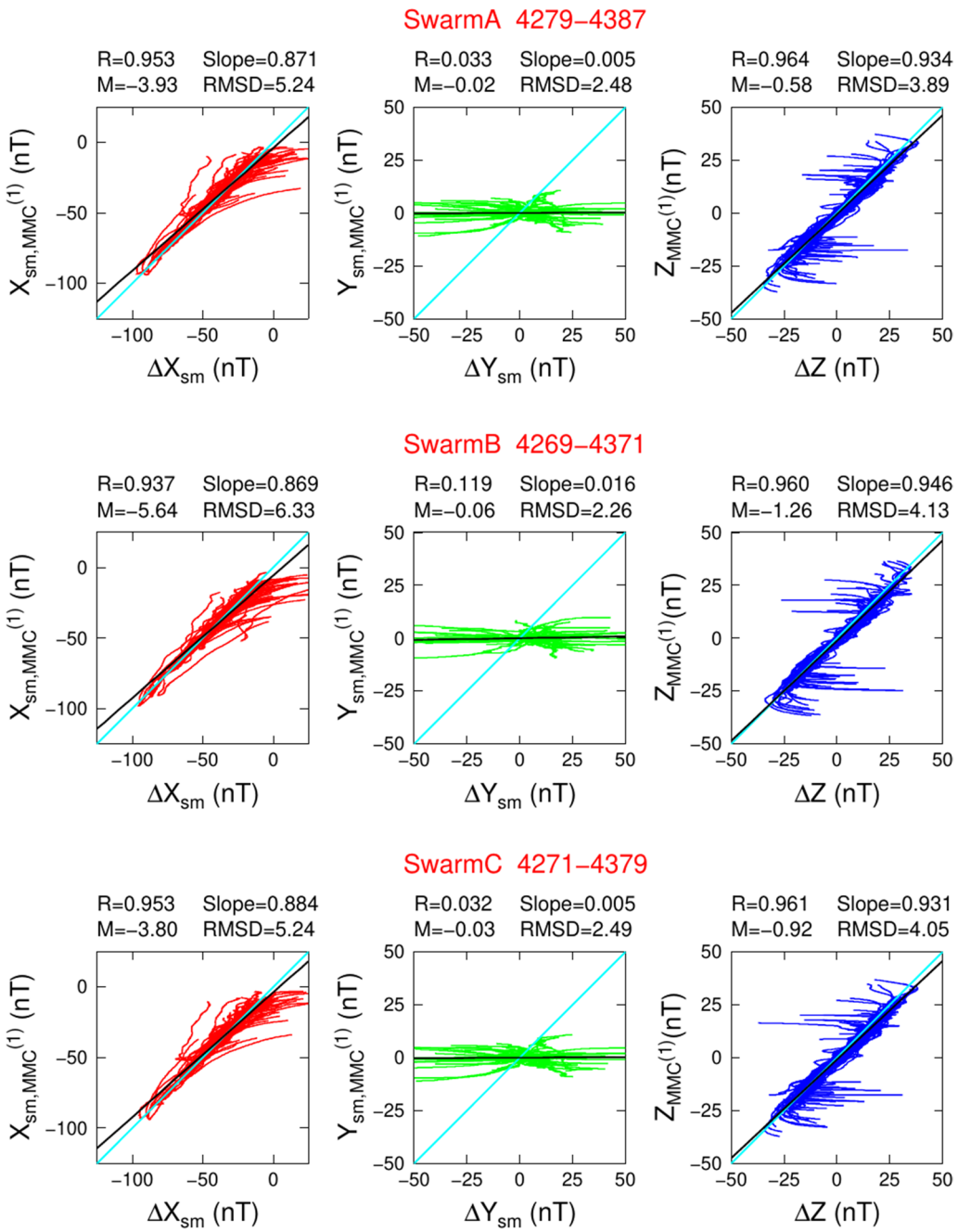

Fig. 5 The same as Figs. 1 and 2, but for the magnetic field components $X^{(1)}_{sm,MMC}$, $Y^{(1)}_{sm,MMC}$ and $Z^{(1)}_{MMC}$ due to the two-circular loop model of MRCs and MICs, and spherical magnetic field residuals ΔX_{sm}, ΔY_{sm} and ΔZ. The magnetic fields of PEJs and FACs have not been removed from Swarm magnetic residuals

Region 1 and 2 (e.g., Iijima and Potemra 1976; Potemra 1983). Region 1 is located at the poleward boundary between the high-conductivity auroral zone and the low-conductivity polar cap, while Region 2 is located near the equatorward edge of the auroral oval. Region 1 field-aligned currents flow into the ionosphere at dawn and out of the ionosphere at dusk while Region 2 field-aligned currents flow out of the ionosphere at dawn and into the ionosphere at dusk.

The auroral electrojets (AEJs) comprise the Hall and Pedersen currents. As shown in Fig. 6, the eastward and westward electrojets are primarily the Hall currents

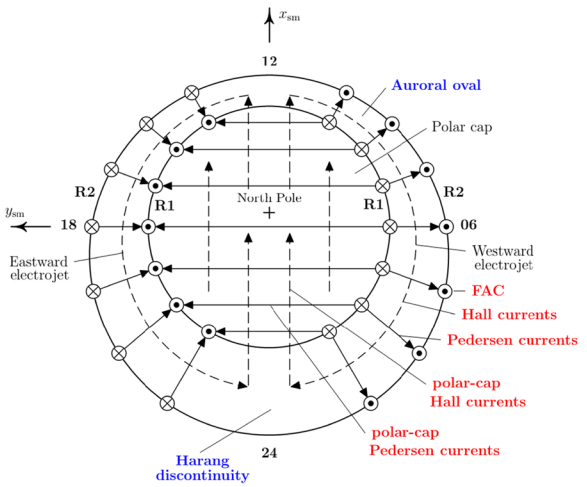

Fig. 6 A schematic view of large-scale current systems in the polar ionosphere of the northern hemisphere. The auroral oval (bounded by two eccentric circles) is the region with an enhanced electrical conductivity. FACs transport energy and momentum between the magnetosphere and ionosphere via Region 1 (the poleward edge of the auroral oval) and Region 2 (the equatorward edge of the auroral oval). Crossed and dotted circles represent the flow of FACs into and out of the ionosphere, respectively. Hall currents and polar-cap Hall currents (dashed lines) flow along the eastward and westward auroral electrojets, and sunwards across the polar cap, respectively. Pedersen currents and polar-cap Pedersen currents (solid lines) flow across the electrojets between Region 1 and Region 2, and across the polar cap to the opposite local-time sector, respectively

which originate around noon and are supplied by downward FACs. The eastward and westward electrojets flow in the afternoon sector, and the morning and midnight sectors, respectively, and terminate in the region of the Harang discontinuity. The Hall currents in the auroral ovals are enclosed by weaker currents that flow sunwards across the low conductivity polar cap. Here, we will called them the polar-cap Hall currents.

The Region 1 and Region 2 field-aligned currents predominantly close via the Pedersen currents across the auroral oval, but can also close via weaker currents across the polar cap (see Fig. 6); we will call them the polar-cap Pedersen currents. In addition, when ionospheric conductivity is nonuniform, the Region 1 and Region 2 currents can close via the Hall currents (Forsyth et al. 2018). The auroral electrojets and polar-cap Hall and Pedersen currents are jointly called the polar electrojets (PEJs). Both the large-scale current systems, the PEJs and FACs, result in magnetic field disturbances of Swarm magnetic measurements.

The Region 1 and Region 2 FACs in Figure 6 are typical when the interplanetary magnetic field (IMF) is directed southward, i.e., when $B_z < 0$ nT. In the other case where the IMF B_z component is northward, an additional FAC current system, known as NBZ (or, Region 0) Birkeland currents, is developed. The NBZ currents are maximised close to local noon at latitudes between the cusp and the pole (e.g., Iijima et al. 1984; Milan et al. 2000). We do not consider these additional currents acting predominantly on daysides because the parameters of electric circuit model are estimated for nightside along-track Swarm data only.

Estimation of the auroral oval locations

The location of the auroral ovals plays an important role in computing the magnetic signature of FACs in the current-free mid-latitude region. The positions of the auroral oval boundaries, that is, Region 1 and Region 2, will be estimated for a single Swarm satellite on track-by-track basis by analysing the Y component of the residuals in SM coordinates, that is, the magnetic field component $\Delta Y_{\rm sm}$. To come to the way of how to do it, we take the following successive thought steps.

Let FACs be first modelled by two semi-infinite long parallel straight wires carrying electric currents I_1 and I_2. Let the wires be placed on a meridional plane $\varphi_{\rm sm} = \varphi_0$ at colatitudes $\vartheta_{\rm sm} = \vartheta_1$ and $\vartheta_{\rm sm} = \vartheta_2$, respectively, and extend from the high-latitude ionosphere to infinity. Let also first assume that a satellite flies along the same meridional plane $\varphi_{\rm sm} = \varphi_0$. The only magnetic field component measured by a satellite onboard magnetometer will be the component perpendicular to the meridional plane, that is, component $Y_{\rm sm}$ in our notation. To follow the FAC case, let the currents carried by the two wires have opposite directions. Then, $Y_{\rm sm}$ between the wires, that is, at colatitudes $\vartheta_{\rm sm} \in (\vartheta_1, \vartheta_2)$, is equal to the sum of the individual contributions $Y^i_{\rm sm}$, $i = 1, 2$, generated by the two wires, while $Y_{\rm sm}$ outside the wires is given by the differences of $Y^i_{\rm sm}$. The same-sign extrema of magnetic field $Y_{\rm sm}$ at satellite altitudes will be located at $\vartheta_{\rm sm} = \vartheta_1$ and $\vartheta_{\rm sm} = \vartheta_2$, respectively. This case is shown in panel A of Fig. 7.

Let us make the first assumption more realistic and consider that the down and up field-aligned currents flow along the field lines of the geomagnetic dipole. This approximation is well valid up to geocentric distances of $\sim 8R_e$ (e.g., Daglis et al. 1999; Tsyganenko 2013). The satellite magnetometer will still measure only component $Y_{\rm sm}$, but, in contrast to the previous case, the same-sign extrema of $Y_{\rm sm}$ will be slightly shifted equatorwards due to the concave field lines of the magnetic dipole. For realistic configurations, the shift is at most 1 degree in colatitude. This case is shown in panel B of Fig. 7.

The second assumption slightly violated for Swarm satellites because they fly along near-polar orbits (the orbit inclinations are approximately 87.4° and 88.0°, respectively). It means that the Swarm onboard magnetometer

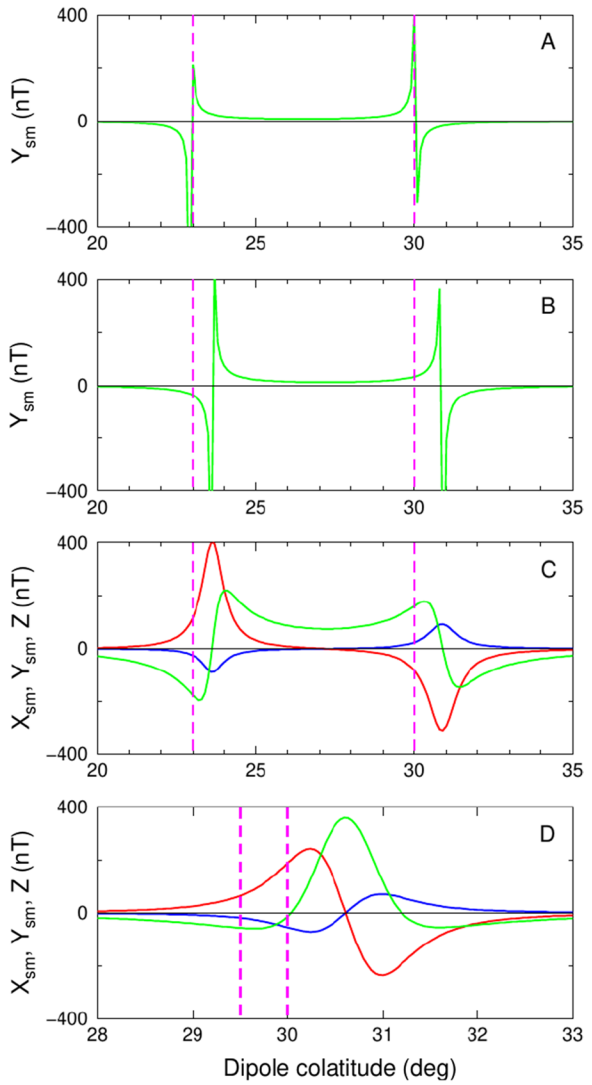

Fig. 7 The magnetic field components X_{sm} (red), Y_{sm} (green) and ΔZ (blue) measured by a satellite vector magnetometer for four hypothetic cases. The vertical dashed violet lines show the position of Region 1 and Region 2. Panel A: A satellite flies in the meridional plane of two semi-infinite long line wires carrying currents of the opposite directions. Panel B: The same as panel A, but the meridional plane contains the down and up field-aligned currents flowing along the field lines of the geomagnetic dipole. Panel C: The same as panel B, but the meridional plane of a satellite orbit is rotated by 2° from the meridional plane of the currents. Panel D: The same as panel C, but the distance between Region 1 and Region 2 is reduced to 0.5°

measures not only the Y_{sm} component but also X_{sm} and Z components of FAC magnetic field. Panel C of Fig. 7 shows this case for the orbit inclination of 88.0°. Important is that the same-sign extrema of component Y_{sm} hardly change their locations; the changes are within 0.3 degree in colatitude. While panel C of Fig. 7 demonstrates the situation at magnetically disturbed times where the width of auroral ovals may reach 10-12 degree in colatitude, panel D of Fig. 7 shows the case at magnetically quiet times where the width of auroral ovals is about 1 degree in colatitude or less. The same-sign extrema of component Y_{sm} are now merged into a single extremum.

The above considerations can be used to estimate the colatitudinal positions of Region 1 and Region 2 along a Swarm satellite track. Because PEJs contribute to Swarm magnetic residual ΔY_{sm} significantly less than FACs, the positions of the same-sign extrema of ΔY_{sm} along a Swarm track in polar regions provide an estimate of the colatitudinal positions of Region 1 and Region 2 for that track. These estimates are to be corrected for up to 1 degree shift equatorward due to the concave field lines of geomagnetic dipole.

Region 1 and Region 2 locations are firstly estimated by a visual inspection of the high-latitude residual signal ΔY_{sm}. Our experience with analysing a large number of along-track Swarm measurements shows that the first visual estimate locates Region 1 and Region 2 within the uncertainty of $\pm 1°$ in colatitude. The visual estimate may be checked and improved, if necessary, by minimising (with respect to the locations of Region 1 and Region 2) the squared mid-latitude differences between $\Delta \boldsymbol{B}^{(1)}_{sm}$ and the magnetic field best-fitting complete-track residuals $\Delta \boldsymbol{B}^{(1)}_{sm}$ by the electric circuit model of PEJs and FACs. This model is presented in the following section.

The example of the estimated locations of Region 1 and Region 2 for the magnetic storm analysed in Fig. 1 is given in Fig. 8. As expected, the position and the width of auroral ovals change in dependence of solar activity. They contract in a narrow region during magnetically quiet conditions and expand into the region of width up to 10° in colatitude during magnetically disturbed times. The uncertainty of the estimated locations of Region 1 and Region 2 is on average about $\pm 0.5°$ in colatitude.

An electric circuit model of PEJs and FACs

The correction of Swarm magnetic residuals $\Delta \boldsymbol{B}^{(1)}_{d}$ due to the magnetic fields generated by PEJs and FACs will by computed for a single Swarm satellite on a track-by-track basis because PEJs and FACs quickly change in time and space at magnetically disturbed times. As introduced, all three Swarm satellites have near-polar orbits. Hence, when a Swarm satellite leaves mid-latitudes it enters the region of an auroral electrojet, say, for example, the westward auroral electrojet, and later the western polar cap (see Fig. 6). We will model the magnetic field generated by the currents flowing only in these two polar regions because their magnetic field contributions to mid-latitude magnetic field are dominant. In other words, the magnetic effect of the currents on the hemisphere opposite to the satellite orbit is considered to be negligible.

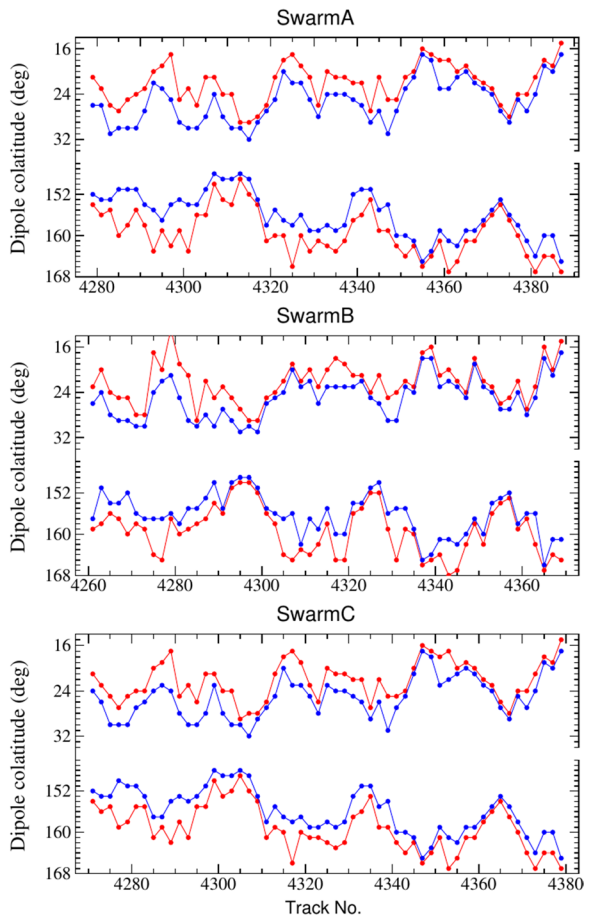

Fig. 8 The colatitudinal positions of Region 1 (red) and Region 2 (blue) of the northern (top part of each panel) and southern (bottom part of each panel) polar ovals for the magnetic storm analysed in Fig. 1. The Region 1 and Region 2 colatitudes were estimated by analysing residual signal $\Delta Y_{\rm sm}$ along Swarm A (top panel), Swarm B (middle panel) and Swarm C (bottom panel) tracks, respectively

Making this assumption is also required by the fact that the inverse problem for the estimation of PEJs and FACs is inherently unstable. Including currents on the hemisphere opposite to the satellite orbit would make the instability even worse.

As shown in Fig. 6, the auroral oval is bounded by two eccentric circles shifted towards midnight by, say, $x_{sm,0}$. The shift $x_{sm,0}$ may be viewed as the fixed input parameter (e.g., 4° towards midnight) for modelling of along-track Swarm data. However, it would not be clear how $x_{sm,0}$ changes from track to track, in particular, during geomagnetic disturbance periods. Alternatively, the shift $x_{sm,0}$ can be included in the list of parameters searching by inversion. Since Swarm data are non-linearly related to $x_{sm,0}$, this parameter should be searched by a grid search, which would increase computational effort rather significantly.

In fact, the non-linear dependence of along-track Swarm data on $x_{sm,0}$ is rather weak for small values of $x_{sm,0}$ which may tend to choose $x_{sm,0}$ ad hoc, e.g., 4°, for all Swarm tracks over a certain magnetic epoch. It would make the mathematical description of an electric circuit model more complex, but the fit of along-track magnetic data will be practically identical as for the choice $x_{sm,0} = 0$. For the sake of simplicity, we therefore choose $x_{sm,0} = 0$ and assume that the auroral oval are bounded by two concentric circles centred at the geomagnetic pole.

In the following two subsections, we will parameterise five systems of currents, that is, the Hall currents, the polar-cap Hall currents, Region 1 and Region 2 field-aligned currents, the Pedersen currents and the polar-cap Pedersen currents, whose magnetic fields are assumed to make the largest contributions to mid-latitude Swarm magnetic residuals. The modelled electric currents will flow along two-dimensional curves and each individual current will have a constant amplitude. The detailed parameterisation of individual currents and the magnetic field generated by them are given in Appendices.

An electric circuit model of Hall currents

Let a satellite cross Region 1 and Region 2 of the auroral oval at colatitudes $\vartheta_{\rm sm,R_1}$ and $\vartheta_{\rm sm,R_2}$, respectively. The horizontal Hall currents in the auroral oval are modelled by a series of $N_{\rm HC}$ steady currents of amplitudes $I^i_{\rm HC}$ flowing along circular arcs in the circle-of-latitude planes of SM colatitudes $\vartheta^i_{\rm HC}$ $i = 1, \ldots, N_{\rm HC}$, which are regularly spaced by $\Delta\vartheta$ over the colatitudinal interval of the auroral oval, that is, $\vartheta_{\rm sm,R_1} < \vartheta^i_{\rm HC} < \vartheta_{\rm sm,R_2}$ at the north and $\vartheta_{\rm sm,R_1} > \vartheta^i_{\rm HC} > \vartheta_{\rm sm,R_2}$ at the south, respectively. Each arc is placed in the horizontal circle-of-latitude plane $z_{\rm sm} = r_{\rm iono}\cos\vartheta^i_{\rm HC}$, has radius $a^i_{\rm HC} = r_{\rm iono}\sin\vartheta^i_{\rm HC}$ and extends over longitude from $-\alpha^i_{\rm HC}$ to $\alpha^i_{\rm HC}$. Here, $r_{\rm iono} = R_e + h_{\rm iono}$, where $h_{\rm iono} = 115\,{\rm km}$ is a height of the approximate location of the E ionospheric region. Because the Hall currents originate around noon and terminate near the Harang discontinuity, we choose $\alpha^i_{\rm HC} = 80°$ for all the currents. The geometry of an individual Hall current is shown in Appendix D.

A circular arc of the Hall current is described by the parametric equations (D.1). The magnetic field generated by a steady electric current flowing along this arc is given by the line integral (A.3) of infinitesimal magnetic field contributions expressed by the Biot–Savart law (B.9). The line integral is calculated by a numerical quadrature over the longitudinal interval $(-\alpha^i_{\rm HC}, \alpha^i_{\rm HC})$.

The inverse problem for estimating the Hall current parameters from Swarm magnetic residuals is unstable (Aakjær et al. 2016). One factor influencing its stability is the size of current spacing $\Delta\vartheta$. The smaller $\Delta\vartheta$, the greater the instability. To trade off stability with resolution, we choose $\Delta\vartheta = 1^\circ$ and kept it fixed. Then, the number of Hall currents lying inside the auroral oval is $N_{\rm HC} = |\vartheta_{{\rm sm},{\rm R}_2} - \vartheta_{{\rm sm},{\rm R}_1}|/\Delta\vartheta + 1$. Since the dimensions of auroral ovals contract or expand in dependence of solar activity, the number of Hall currents, $N_{\rm HC}$, will change from track to track, and will differ for the northern and southern auroral ovals.

The polar-cap Hall currents flowing sunwards across the polar cap are modelled by a series of $N_{\rm HC}$ steady currents $I^i_{\rm PHC}$ flowing in the $y_{\rm sm} = y^i_{\rm PHC}$ planes, $y^i_{\rm PHC} = a^i_{\rm HC}\cos\alpha^i_{\rm HC}$, $i = 1,\ldots,N_{\rm HC}$, along circular arcs of radius $r_{\rm iono}$. The arcs extend from $-\beta^i_A$ to β^i_A, where β^i_A is given by (E.7), $\sin\beta^i_A = \sin\vartheta^i_A\sin\alpha^i_A$. The geometry of an individual polar-cap Hall current is shown in Appendix 10.

Note that we have chosen the number of the polar-cap Hall currents equal to the number of the Hall currents such that they form closed electric circuits in the polar ionosphere. However, because the conductivity of auroral ovals is larger than the conductivity of polar cap, the amplitudes $I^i_{\rm HC}$ and $I^i_{\rm PHC}$ generally differ and constitute two sets of model parameters to be estimated for each satellite track.

A circular arc of the polar-cap Hall current is described by the parametric equations (E.1). The magnetic field generated by a steady electric current flowing along this arc is given by the line integral (A.3) of infinitesimal magnetic field contributions expressed by the Biot–Savart law (E.2). The line integral is calculated numerically over angles from $-\beta^i_A$ to β^i_A.

An electric circuit model of FACs and Pedersen currents

The field-aligned currents entering or leaving Region 1 and Region 2 are modelled by a series of $2N_{\rm FAC}+1$ steady currents of amplitudes $I^i_{\rm FAC}$ flowing in the meridian planes of SM longitudes $\varphi^i_{\rm FAC}$, $i = 1,\ldots,2N_{\rm FAC}+1$, along the dipole field lines (I.3) between Region 1 or Region 2 and the dipole equatorial plane. The geometry of an individual pair of Region 1 and Region 2 field-aligned currents connecting the northern polar ionosphere and the inner magnetosphere is shown in Appendix I. The meridian planes are regularly spaced around the satellite longitude $\varphi^{\rm sat}_{\rm sm}$ by a constant angle $\Delta\varphi$ such that $\varphi^i_{\rm FAC} = \varphi^{\rm sat}_{\rm sm} + (-N_{\rm FAC} + i - 1)\Delta\varphi$, $i = 1,\ldots,2N_{\rm FAC}+1$. We choose $\Delta\varphi = 1^\circ$ due to the same reason as the choice $\Delta\vartheta = 1^\circ$ for the spacing of the Hall currents. To make the inverse problem for estimating FACs and PEJs better controlled, we choose the same number of FACs entering or leaving Region 1 or Region 2 for both the northern and the southern polar ionospheres. The magnetic field generated by a steady electric current flowing along a dipole field line is given by the line integral (A.3) of infinitesimal magnetic field contributions expressed by the Biot–Savart law (G.6) after substituting eqs (I.4) and (I.5). The line integral is calculated by a numerical quadrature over the colatitudinal interval $(\vartheta_{{\rm sm},{\rm R}_1}, 90^\circ)$ or $(\vartheta_{{\rm sm},{\rm R}_2}, 90^\circ)$.

The horizontal Pedersen currents inside the auroral oval are modelled by a series of $2N_{\rm PC}+1$ steady currents $I^i_{\rm PC}$ flowing in the meridian planes of SM longitudes $\varphi^i_{\rm PC}$, $i = 1,\ldots,2N_{\rm PC}+1$, along circular arcs of radius $r_{\rm iono}$ between the upward and downward FACs, that is, between Region 1 and Region 2. The geometry of an individual Pedersen current is shown in Appendix H.

The meridian planes are again regularly spaced around the satellite longitude by a constant angle $\Delta\varphi = 1^\circ$ such that $\varphi^i_{\rm PC} = \varphi^{\rm sat}_{\rm sm} + (-N_{\rm PC} + i - 1)\Delta\varphi$, $i = 1,\ldots,2N_{\rm PC}+1$.

We have chosen the number of Pedersen currents smaller than the number of FACs ($N^{\rm PC} < N^{\rm FAC}$) because the design matrix $\boldsymbol{G}$ (see the next section) is quickly getting ill-posed with increasing $N^{\rm PC}$ while the conditionality of $\boldsymbol{G}$ with increasing $N^{\rm FAC}$ does not degrade so quickly. A circular meridian arc of the Pedersen current is described by the parametric equations (H.1). The magnetic field generated by a steady electric current flowing along this circular arc is given by the line integral (A.3) of infinitesimal magnetic field contributions expressed by the Biot–Savart law (G.6) after substituting eqs (H.2) and (H.3). The line integral is calculated by a numerical quadrature over the colatitudinal interval $(\vartheta_{{\rm sm},{\rm R}_1}, \vartheta_{{\rm sm},{\rm R}_2})$.

Finally, the polar-cap Pedersen currents flowing across the polar cap are modelled by a series of $2N_{\rm PC}+1$ steady currents $I^i_{\rm PPC}$ flowing along circular arcs lying in the $x_{\rm sm} = x^i_{\rm PPC}$ planes, $x^i_{\rm PPC} = r_{\rm iono}\sin\vartheta_{{\rm R}_1}\sin\varphi^i_{\rm PC}$, $i = 1,\ldots,2N_{\rm PC}+1$; each arc has radius $r_{\rm iono}$. The arcs extend over angles from $-\gamma^i_C$ to γ^i_C, where γ^i_C is given by (F.7), $\sin\gamma^i_C = \sin\vartheta_{{\rm R}_1}\cos\varphi^i_{\rm PC}$. The geometry of an individual polar-cap Pedersen current is shown in Appendix F.

To make the inverse problem for the estimation of FACs and PEJs easier to control, we choose the number of the polar-cap Pedersen currents equal to the number of the Pedersen currents. The polar-cap Pedersen currents should close via the field-aligned currents in the opposite local-time sector. As we assume, however, we consider the magnetic effect of those 'opposite' currents on the mid-latitude magnetic data negligible with respect to the magnetic effects of the PEJs and FACs flowing in the vicinity of the satellite orbit.

A circular arc of the polar-cap Pedersen current is described by the parametric equations (F.1). The magnetic field generated by a steady electric current flowing along this circular arc is given by the line integral (A.3) of infinitesimal magnetic field contributions expressed by the Biot–Savart law (F.2). The line integral is calculated by a numerical quadrature over angles from $-\gamma_{\rm C}^i$ to $\gamma_{\rm C}^i$.

Estimation of PEJ and FAC current amplitudes

Denoting $n_{\rm FAC}=2N_{\rm FAC}+1$ and $n_{\rm PC}=2N_{\rm PC}+1$, the total number of the amplitudes of PEJs and FACs at the northern and southern polar ionospheres are, respectively, $N^{\rm n}=2N_{\rm HC}^{\rm n}+2n_{\rm FAC}+2n_{\rm PC}$ and $N^{\rm s}=2N_{\rm HC}^{\rm s}+2n_{\rm FAC}+2n_{\rm PC}$, where the superscripts 'n' and 's' stand for 'north' and 'south', respectively. These numbers correspond to our choice of circuit model parameterisation. The numbers of Hall currents differ for the northern and southern polar ionospheres because they are determined by the widths of the northern and southern auroral ovals which may differ in dimensions. On the other hand, we choose the same number of FACs and Pedersen currents at the northern and southern polar regions. In total, the number of the amplitudes of PEJs and FACs for both polar ionospheres is $N=N^{\rm n}+N^{\rm s}$.

The amplitudes of PEJs and FACs will be estimated from the D samples of magnetic residuals $\Delta X_{\rm sm}^{(1)}$, $\Delta Y_{\rm sm}^{(1)}$ and $\Delta Z^{(1)}$ at locations $\boldsymbol{r}_s=(r_s,\vartheta_{{\rm sm},s},\varphi_{{\rm sm},s})$ along a complete Swarm track. They satisfy the observation equation of the form

$$\boldsymbol{d}=\boldsymbol{G}\boldsymbol{m}+\boldsymbol{e}, \tag{7}$$

where $\boldsymbol{d}$ is the column vector of $3D$ data samples,

$$\boldsymbol{d}=\{\big(\Delta X_{\rm sm}^{(1)}(\boldsymbol{r}_s),\Delta Y_{\rm sm}^{(1)}(\boldsymbol{r}_s),\Delta Z^{(1)}(\boldsymbol{r}_s)\big)^T,\ s=1,2,\ldots,D\}, \tag{8}$$

'T' stands for transposition, $\boldsymbol{m}=(\boldsymbol{m}^{\rm n},\boldsymbol{m}^{\rm s})^T$ is the column vector of $N^{\rm n}+N^{\rm s}$ amplitudes of PEJs and FACs,

$$\begin{aligned}\boldsymbol{m}^{\rm n}=\{&\big(I_{\rm HC}^{i,{\rm n}},I_{\rm PHC}^{i,{\rm n}},I_{\rm FAC,R1}^{j,{\rm n}},I_{\rm FAC,R2}^{j,{\rm n}},I_{\rm PC}^{k,{\rm n}},I_{\rm PPC}^{k,{\rm n}}\big),\\ &i=1,\ldots,N_{\rm HC}^{\rm n},j=1,\ldots,N_{\rm FAC},k=1,\ldots,N_{\rm PC}\},\end{aligned} \tag{9}$$

$$\begin{aligned}\boldsymbol{m}^{\rm s}=\{&\big(I_{\rm HC}^{i,{\rm s}},I_{\rm PHC}^{i,{\rm s}},I_{\rm FAC,R1}^{j,{\rm s}},I_{\rm FAC,R2}^{j,{\rm s}},I_{\rm PC}^{k,{\rm s}},I_{\rm PPC}^{k,{\rm s}}\big),\\ &i=1,\ldots,N_{\rm HC}^{\rm s},j=1,\ldots,N_{\rm FAC},k=1,\ldots,N_{\rm PC}\},\end{aligned} \tag{10}$$

the subscripts 'R1' and 'R2' stand for 'Region 1' and 'Region 2', respectively. The design matrix $\boldsymbol{G}$ is composed of three block matrices each of which is associated with one component of the magnetic residuals $\boldsymbol{d}$,

$$\boldsymbol{G}=\{\boldsymbol{G}_X,\boldsymbol{G}_Y,\boldsymbol{G}_Z\}^T. \tag{11}$$

The elements of block matrices are

$$(\boldsymbol{G}_{X,Y,Z})_{s,\ell}=\int_{\alpha'_\ell}dB_{X,Y,Z}(\boldsymbol{r}_s,\boldsymbol{p}_\ell)d\alpha', \tag{12}$$

where $s=1,2,\ldots,D$, and ℓ runs over all indices i, j and k as in eqs (9) and (10). The infinitesimal magnetic field contributions $dB_{X,Y,Z}$ are given by the Biot–Savart law specified for an individual PEJ or FAC in Appendices. Each current is described by a set of parameters $\boldsymbol{p}_\ell$ and the bounds α'_ℓ of line integral (12). For example, $dB_{X,Y,Z}$ for the Hall current is given by Eq. (B.9) that is transformed from Cartesian coordinates to spherical coordinates by Eq. (B.10). Besides the radius of ionosphere, $r_{\rm iono}$, and the colatitudes of Region 1 and Region 2, $\vartheta_{{\rm sm},{\rm R}_1}$ and $\vartheta_{{\rm sm},{\rm R}_2}$, each Hall current is specified by colatitude $\vartheta_{\rm HC}^\ell$; the line integral 12 is carried out over longitudes from $-\alpha_{\rm HC}^\ell$ to $\alpha_{\rm HC}^\ell$. The parameters $\boldsymbol{p}_\ell$ and bounds α'_ℓ of the other PEJs and FACs have been given in the previous two sections.

Because of data errors and other possible contributions to Swarm magnetic residuals, both expressed by $\boldsymbol{e}$, Eq. (7) is mathematically inconsistent and an exact solution to this system does not exist. The estimate $\hat{\boldsymbol{m}}$ of model parameters $\boldsymbol{m}$ by the least-squares is given by the normal equations (e.g., Koch 1999)

$$\boldsymbol{G}^T\boldsymbol{G}\,\hat{\boldsymbol{m}}=\boldsymbol{G}^T\boldsymbol{d}. \tag{13}$$

Though the normal equations are consistent, there are still two problems related to them. In fact, given along-track magnetic residual values can be generated by more than one current distributions. We have reduced this non-uniqueness by a priori choice of the geometry of large-scale current systems in the polar ionospheres, but the number of the currents in each system is still to be chosen to specify estimate $\hat{\boldsymbol{m}}$ uniquely. Hence, the choice of size N of the $N\times N$ matrix $\boldsymbol{G}^T\boldsymbol{G}$ makes the problem non-unique. However, there is no unique prescription on the number N of model parameters $\boldsymbol{m}$. We will follow a rule of thumb recommending that a linear regression should be carried out for, at least, 10-20 observations for each independent parameter (e.g., Austin and Steyerberg 2015). We use the Swarm vector magnetic measurements with a time step of 1 s such that each track contains approximately 2800 observations. According to the rule of thumb, the recommended number of parameter $\hat{\boldsymbol{m}}$ for the least-squares applied to the observations along each track is about 140–280.

The second problem arises due to the instability of a least-squares solution. This inherent property reflects the fact that the magnetic field decreases with increasing distance from a source current. It is therefore an unstable problem to look for a source current from the magnetic field observations in regions farther from the source

because a small error in magnetic observations may be interpreted by large source currents.

There is a number of ways to regularise ill-conditioned matrix $\boldsymbol{G}^T\boldsymbol{G}$ (e.g., Menke 2012). Here, we choose a simple (or zeroth-order) Tikhonov regularisation (Tikhonov 1963) by adding positive elements to its diagonals. The regularised least-squares estimate $\hat{\boldsymbol{m}}$ of model parameters $\boldsymbol{m}$ is then

$$\hat{\boldsymbol{m}} = (\boldsymbol{G}^T\boldsymbol{G} + \alpha^2\boldsymbol{I})^{-1}\boldsymbol{G}^T\boldsymbol{d}, \tag{14}$$

where $\boldsymbol{I}$ is the identity matrix and α^2 is the regularisation parameter controlling the strength of the regularisation. Again, there is no unique prescription on the size of α^2. In general, α^2 should be chosen such that a desired trade-off between data misfit and model resolution (or complexity) is achieved.

Figure 9 plots the norm of vector $\hat{\boldsymbol{m}}$ (individually normalised by the number of parameters N for better comparison between different tracks) as a function of the norm of the data-misfit vector $\boldsymbol{d} - \boldsymbol{G}\hat{\boldsymbol{m}}$ in the so-called L-curve (Hansen 1992) for six selected Swarm A tracks (see Table 1). According to Hansen (1992), the optimal regularisation parameter α^2 is chosen visually in, or near, the corner of the L-curve. The corner value of α^2 between 1×10^{-11} nT^{2}A^{-2} and 3×10^{-11} nT^{2}A^{-2} seems to balance the data misfit and model resolution. Choosing $\alpha^2 = 2 \times 10^{-11}$ nT^{2}A^{-2}, Fig. 10 shows the magnetic residuals $\Delta X_{\rm d}^{(1)}$, $\Delta Y_{\rm d}^{(1)}$ and $\Delta Z^{(1)}$ and their fits by the regularised linear least squares for the six selected Swarm A tracks during magnetically stormy conditions. A visual inspection reveals rather large differences between the data and their fits. This is, in particular, unwanted feature at mid-latitudes because the mid-latitude residuals after their fitting by the magnetic fields of PEJs and FACs will be used, in the next step, for the estimation of MMF.

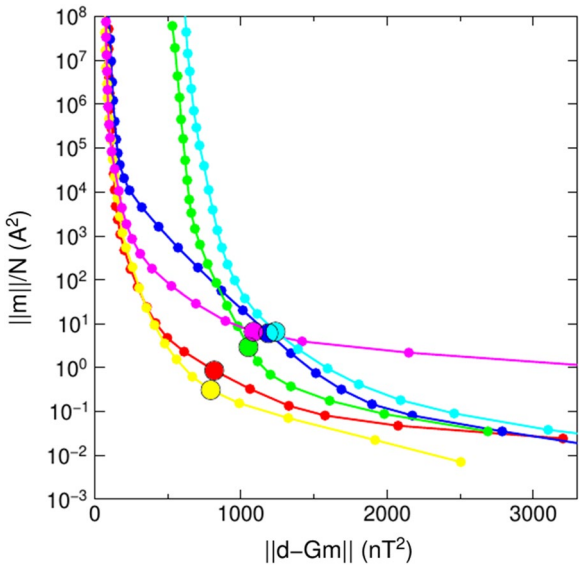

Fig. 9 Trade-off curves between data misfit and model resolution (the L-curves) for six selected Swarm A tracks (see Table 1). Red, blue, green, yellow, violet and light blue stand for tracks A4301, A4855, A4975, A5097, A8506 and A9012, respectively. The dotes denote chosen values of the regularisation parameter α^2 in the range between 1×10^{-19} nT^{2}A^{-2} and 1×10^{-8} nT^{2}A^{-2}. The corner values of the L-curves occur for α^2 between 1×10^{-11} nT^{2}A^{-2} and 3×10^{-11} nT^{2}A^{-2}. The common value of α^2 used for the analysis of the along-track data in Fig. 10 was chosen equal to $\alpha^2 = 2 \times 10^{-11}$ nT^{2}A^{-2} (large circles). The norm of vector $\boldsymbol{m}$ is normalised by the number of model parameters N for better comparison between different tracks

A rather poor fit is caused by a too large value of the regularisation parameter α^2. To get a better fit of data, the value of α^2 needs to be decreased. Because the mid-latitude residuals are interpreted in the next processing step, we will decrease a value of α^2 such that the data misfit over mid-latitudes is decreased. Figure 11 plots the L-curves between the mid-latitude data-misfit vector $(\boldsymbol{d} - \boldsymbol{G}\hat{\boldsymbol{m}})_{\rm ML}$ and the norm of vector $\hat{\boldsymbol{m}}$ for six selected Swarm A tracks. The corner value of L-curves for α^2 between 1×10^{-14} nT^{2}A^{-2} and 1×10^{-15} nT^{2}A^{-2} balance the mid-latitude data misfit and the model resolution. Figure 12 plots the magnetic residuals $\Delta X_{\rm d}^{(1)}$, $\Delta Y_{\rm d}^{(1)}$ and $\Delta Z^{(1)}$ and their fits by the regularised linear least squares for a common choice of $\alpha^2 = 3 \times 10^{-15}$ nT^{2}A^{-2} and for the six Swarm A tracks analysed in Fig. 10. The comparison of the two figures shows that the regularised linear least squares for $\alpha^2 = 3 \times 10^{-15}$ nT^{2}A^{-2} adjusts, as expected, the data much closer (not only those over mid-latitudes). The price paid for decreasing a value of α^2 to 3×10^{-15} nT^{2}A^{-2}, that is, making the least squares less stable but having a better resolution, is manifested in Fig. 12 by small-scale oscillations of a fit in polar regions. Because only mid-latitude data and their fit are used in the next processing step, we do not need to deal with this unphysical noise.

The model scheme of AEJs and FACs idealises the real situation. For example, the amplitudes of individual currents are considered space and time independent such that the model satisfies the local current continuity constraint $\operatorname{div} I = 0$. However, the current continuity at the points of conjunction between various currents is not required. For example, at the conjunction between FAC and ionospheric currents in Fig. 20, it would probably demand that the downward FAC at point C feeds both $I_{\rm PC}$ and $I_{\rm PPC}$, and the strength of the FAC is determined as

$$I_{\rm FAC} = I_{\rm PC} + I_{\rm PPC}. \tag{15}$$

A reason to abandon such a current continuity constraint is due to the fact the Swarm data used to estimate the current amplitudes are considered along a complete

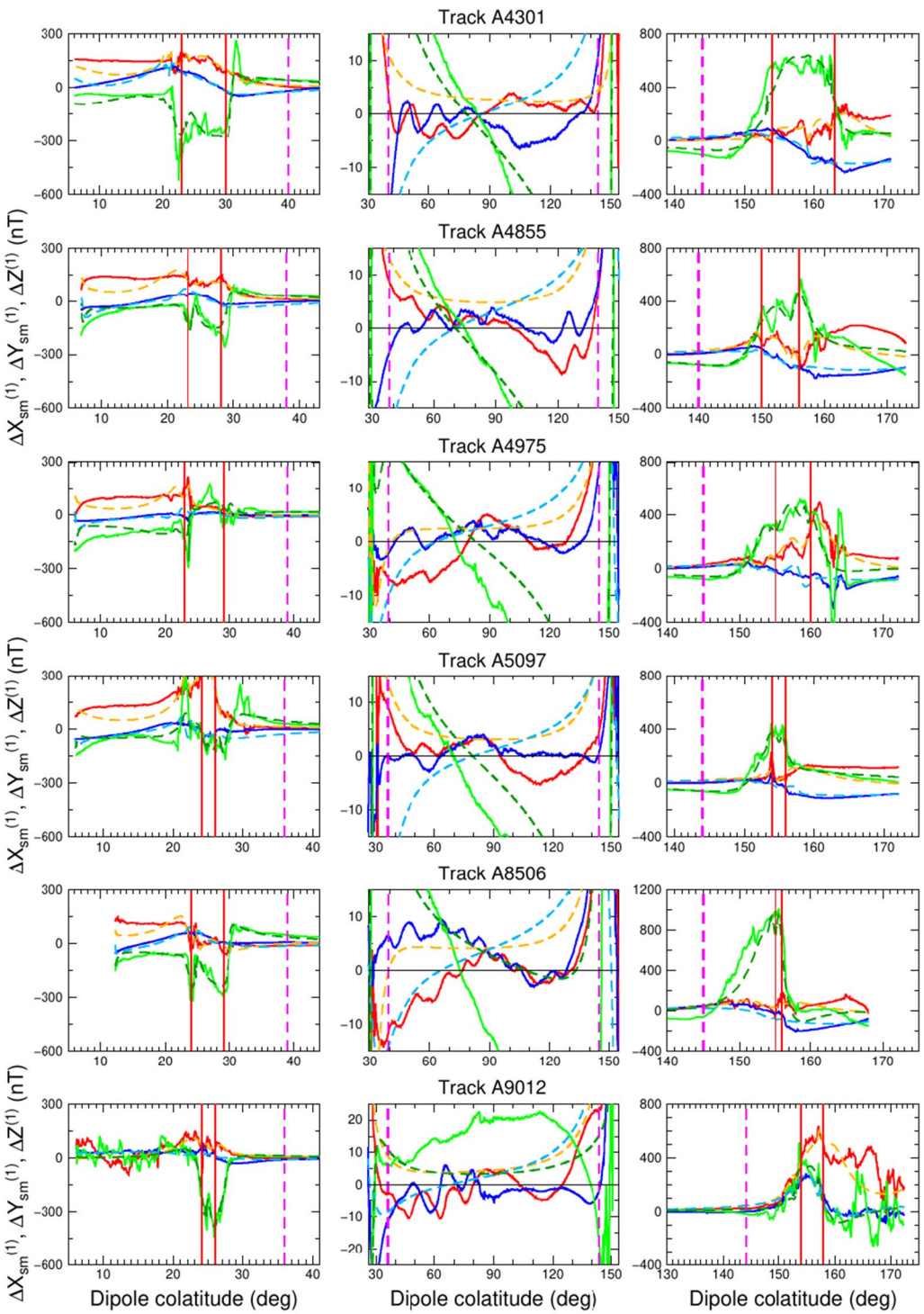

Fig. 10 The Swarm residuals $\Delta X_{sm}^{(1)}$ (solid red), $\Delta Y_{sm}^{(1)}$ (solid green) and $\Delta Z^{(1)}$ (solid blue) along six Swarm A nightside full tracks (see Table 1) and their best fits by the regularised linear least squares (dashed lines) for $\alpha^2 = 2 \times 10^{-10}\,\mathrm{nT^2A^{-2}}$. The left, middle and right columns stand for the northern polar region, mid-latitudes and southern polar region, respectively. The vertical red lines in the left-hand and right-hand panels denote the estimated positions of the northern and southern auroral ovals, respectively; see Fig. 8. The mid-latitudes ranges between colatitudes $\vartheta_{\mathrm{sm},R_2^n} + 10°$ and $\vartheta_{\mathrm{sm},R_2^s} - 10°$ (vertical dashed violet lines)

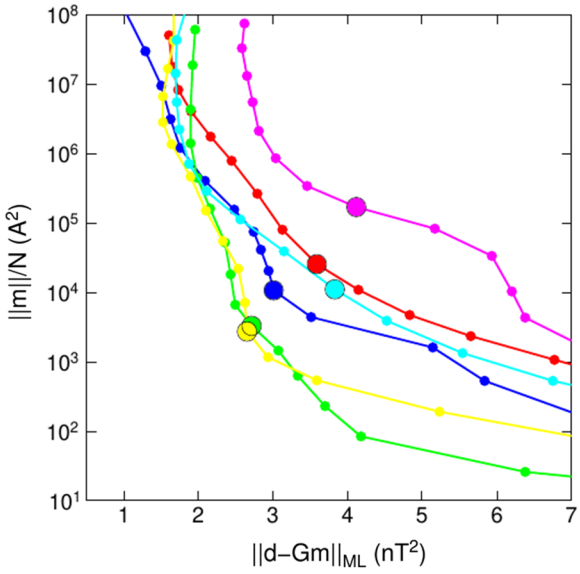

Fig. 11 The same as Fig. 9, but for the mid-latitude residuals $(\boldsymbol{d} - \boldsymbol{G}\hat{\boldsymbol{m}})_{\mathrm{ML}}$. The common value of α^2 used for the analysis all Swarm data was chosen equal to $\alpha^2 = 3 \times 10^{-15}\,\mathrm{nT^2A^{-2}}$ (large circles)

Swarm track of 45 min duration. It is not clear to the authors how the current continuity constraint should be modified over a non-zero time interval, in particular, over geomagnetic disturbance periods when 15 holds at a particular time instant but could be significantly violated for 45 min interval. However, if a time-average current continuity constraint is specified, it can be implemented in a future version of the model. A helpful note on current closure for the Biot–Savart law is given by Vasyliūnas (1999).

A revised estimate of MMF

In "Electric two-circular loop model of MRCs and MICs" section, the MMF was estimated directly from 'raw' mid-latitude residuals ΔX_{sm} and ΔZ without removing the magnetic fields of PEJs and FACs. Because those fields were estimated in the previous sections, we will now remove them from residuals ΔX_{sm} and ΔZ (and also ΔY_{sm}) and estimate the MMF once again in terms of the same model as in "Electric two-circular loop model of MRCs and MICs" section, that is, a two-circular loop model of MRCs and MICs. In contrast to the previous case, we adjust not only ΔX_{sm} and ΔZ, but also ΔY_{sm}, all reduced for the magnetic fields of PEJs and FACs.

Let the magnetic field generated by the electric circuit model of PEJs and FACs best fitting the full-track residuals $\boldsymbol{B}^{(1)}_{\mathrm{sm}}$ be denoted as $\boldsymbol{B}_{\mathrm{sm,PF}}$. In component form, $\boldsymbol{B}_{\mathrm{sm,PF}}$ can be expressed as

$$\begin{aligned}\boldsymbol{B}_{\mathrm{sm,PF}}(r,\Omega_{\mathrm{sm}},t) = &- Z_{\mathrm{PF}}(r,\Omega_{\mathrm{sm}},t)\boldsymbol{e}_r \\ &- X_{\mathrm{sm,PF}}(r,\Omega_{\mathrm{sm}},t)\boldsymbol{e}_{\vartheta_{\mathrm{sm}}}, \\ &+ Y_{\mathrm{sm,PF}}(r,\Omega_{\mathrm{sm}},t)\boldsymbol{e}_{\varphi_{\mathrm{sm}}}.\end{aligned} \tag{16}$$

A new residual magnetic field $\Delta\boldsymbol{B}^{(2)}_{\mathrm{sm}}$ is defined by subtracting $\boldsymbol{B}_{\mathrm{sm,PF}}$ from the original residuals $\Delta\boldsymbol{B}_{\mathrm{sm}}$,

$$\Delta\boldsymbol{B}^{(2)}_{\mathrm{sm}} = \Delta\boldsymbol{B}_{\mathrm{sm}} - \boldsymbol{B}_{\mathrm{sm,PF}}, \tag{17}$$

where $\Delta\boldsymbol{B}_{\mathrm{sm}}$ is given by Eq. (3).

We again group magnetic residuals $\Delta X^{(2)}_{\mathrm{sm}}$, $\Delta Y^{(2)}_{\mathrm{sm}}$ and $\Delta Z^{(2)}$ in discrete time bins of 1 hour duration and use the electric circuit model of MRCs and MICs to adjust the grouped residuals in each time bin. The electric circuit model of MRCs and MICs, presented in "Electric two-circular loop model of MRCs and MICs" section, is composed of two circular loops lying on the dipole equatorial plane (i.e., $x_{\mathrm{sm}}y_{\mathrm{sm}}$ plane). The circles are again shifted along the x_{sm} axis. The model is represented by 6 parameters, that is, radii a_e and a_i of the external and internal circles, shifts x_{0e} and x_{0i} of the circles along the x_{sm} axis and steady electric currents I_e and I_i flowing along the circles. The 6 parameters representing the MMF in a time bin are searched in the same way as in "Electric two-circular loop model of MRCs and MICs" section, that is, the non-linear inversion of residuals $\Delta X^{(2)}_{\mathrm{sm}}$, $\Delta Y^{(2)}_{\mathrm{sm}}$ and $\Delta Z^{(2)}$ for estimating geometric parameters a_e, x_{0e}, a_i, x_{0i} is solved by a grid search over a specified range of parameters given by Eq. (4), while the amplitudes of electric currents, I_e and I_i, are estimated by least squares.

Figure 13 shows the time evolution of external parameters I_e, a_e and x_{0e}, and internal parameters I_i, a_i and x_{0i} of magnetospheric magnetic field model MMC best fitting residuals $\Delta X^{(2)}_{\mathrm{sm}}$, $\Delta Y^{(2)}_{\mathrm{sm}}$ and $\Delta Z^{(2)}$ in each time bin for the magnetic storm analysed in Fig. 1. We can see that the geometric parameters are quickly changing in time within the the ranges specified a priori by constraints (4). Since electric current amplitudes I_e and I_i have been estimated by least squares, we test their statistical significance by Student's t-test (e.g., Martinec et al. 2018). Under the assumption that errors contaminating residuals $\Delta X^{(2)}_{\mathrm{sm}}$, $\Delta Y^{(2)}_{\mathrm{sm}}$ and $\Delta Z^{(2)}$ are random and normally distributed, Student's t-test, performed for each time bin, has showed (not presented here) that all amplitudes I_e and I_i are statistically significant. The test results should be considered with caution because the assumptions of testing may be compromised for the residuals adjusted.

Having found the 6 parameters in each time bin, the MMF is calculated along all Swarm tracks belonging to the time bin. The functionality of MRC–MIC model is evaluated by inspecting the differences between residuals $\Delta X^{(2)}_{\mathrm{sm}}$, $\Delta Y^{(2)}_{\mathrm{sm}}$ and $\Delta Z^{(2)}$ and the best-fitting

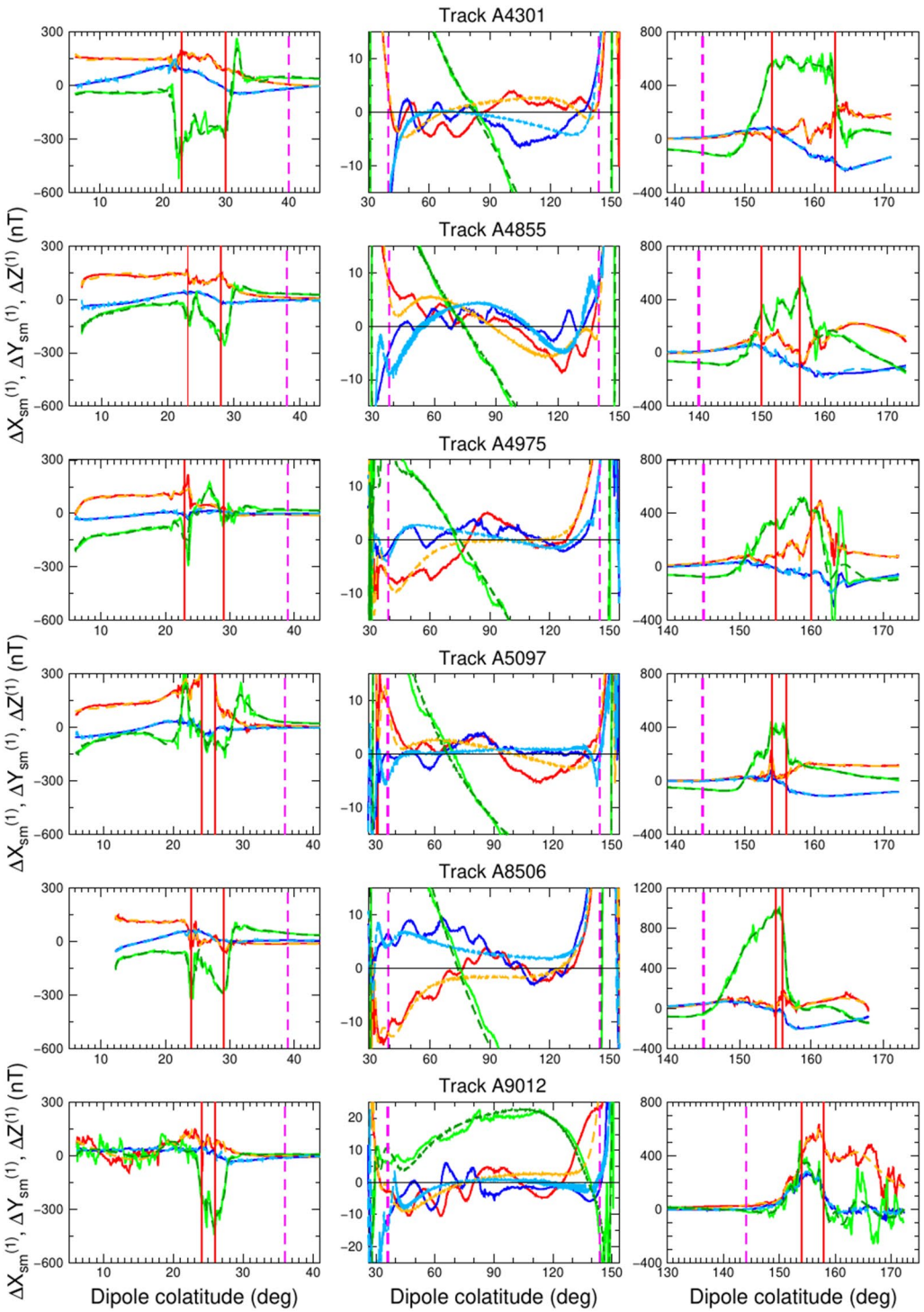

Fig. 12 The same as Fig. 10, but for $\alpha^2 = 3 \times 10^{-15}\,\mathrm{nT^2A^{-2}}$

magnetospheric magnetic fields $X^{(2)}_{\mathrm{sm,MMC}}$, $Y^{(2)}_{\mathrm{sm,MMC}}$ and $Z^{(2)}_{\mathrm{MMC}}$. In contrast to model $X^{(1)}_{\mathrm{sm,MMC}}$ and $Z^{(1)}_{\mathrm{MMC}}$, label '(2)' indicates that $X^{(2)}_{\mathrm{sm,MMC}}$, $Y^{(2)}_{\mathrm{sm,MMC}}$ and $Z^{(2)}_{\mathrm{MMC}}$ are the estimates of MMF based on the mid-latitude residuals that are corrected for the magnetic fields of PEJs and FACs, and subsequently grouped in discrete time bins of 1 hour duration.

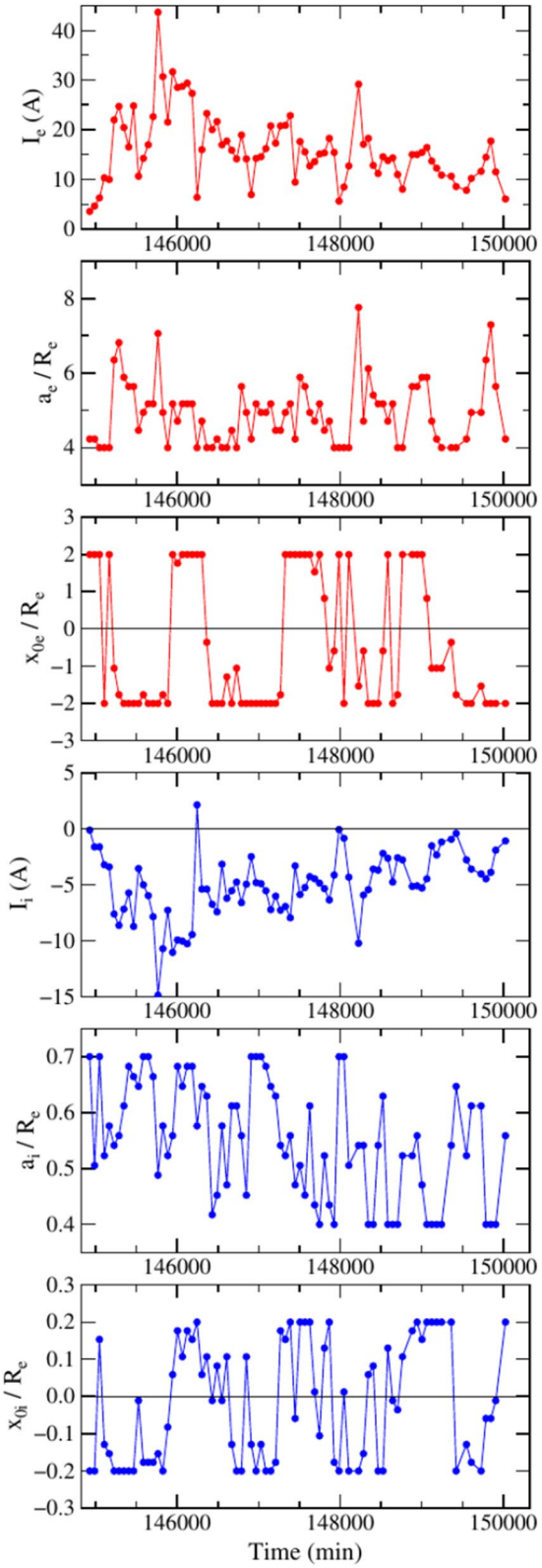

Fig. 13 The time evolution of external parameters I_e, a_e and x_{0e} (red) and internal parameters I_i, a_i and x_{0i} (blue) of model MMC best-fitting residuals $\Delta X^{(2)}_{\rm sm}$, $\Delta Y^{(2)}_{\rm sm}$ and $\Delta Z^{(2)}$ in each time bin. Time span covers the magnetic storm analysed in Fig. 1

Figure 14 demonstrates for six selected Swarm A tracks (see Table 1) that the two-circle model captures mid-latitude residuals $\Delta X^{(2)}_{\rm sm}$, $\Delta Y^{(2)}_{\rm sm}$ and $\Delta Z^{(2)}$ again solidly well as it does, for different values of parameters $a_e, x_{0e}, a_i, x_{0i}, I_e$ and I_i, for mid-latitude residuals $\Delta X_{\rm sm}$ and ΔZ in Fig. 4. However, the comparison of the right panels of Figs. 4 and 14 reveals that the differences between the data and their fits are smaller in the latter, which means that the revised model MMC$^{(2)}$ provides a more reliable estimate of MMF than model MMC$^{(1)}$. This is also confirmed by the comparison of the scatter diagrams plotted in Figs. 5 and 15 (see below).

Figure 15 shows the scatter plots between residuals $\Delta X^{(2)}_{\rm sm}$, $\Delta Y^{(2)}_{\rm sm}$ and $\Delta Z^{(2)}$ and the best-fitting magnetospheric magnetic fields $X^{(2)}_{\rm sm,MMC}$, $Y^{(2)}_{\rm sm,MMC}$ and $Z^{(2)}_{\rm MMC}$ for the moderate magnetic storm analysed in Fig. 5. Comparing Figs. 5 and 15, we can see that model MMC$^{(2)}$ performs significantly better than model MMC$^{(1)}$ in all three magnetic field components. For example, $R \approx 0.962$, $S \approx 0.940$, $M \approx -0.92$ nT and RMSD ≈ 4.06 nT for the Z component of MMC$^{(1)}$, while $R \approx 0.992$, $S \approx 0.983$, $M \approx -0.10$ nT and RMSD ≈ 1.98 nT for the Z component of MMC$^{(2)}$. Similarly, $R \approx 0.947$, $S \approx 0.873$, $M \approx -4.46$ nT and RMSD ≈ 5.60 nT for the X component of MMC$^{(1)}$, while $R \approx 0.992$, $S \approx 0.976$, $M \approx -0.99$ nT and RMSD ≈ 2.14 nT for the X component of MMC$^{(2)}$. All three sets of scatter plots in Fig. 15 show that long-wavelength signals are well modelled by the complex circuit model of electric currents in the polar ionosphere, magnetosphere and between the two regions. In other words, removing the magnetic disturbing effect of PEJs and FACs from Swarm residuals improves significantly the estimate of MMF.

In addition, comparing scatter plots in Figs. 1 and 15, we can see that model MMC$^{(2)}$ provides the estimate of MMF with a significantly better linear fit and a smaller scatter of Swarm residuals than model MMA (Sabaka et al. 2020). Hence, removing the magnetic fields of PEJs and FACs before estimating the MMF is a crucial step for improving the quality of the existing models of MMF (Sabaka et al. 2020; Martinec et al. 2018).

Spherical harmonic coefficients of MMF

Having determined 3×2 electric current parameters representing a new magnetospheric magnetic field model MMC$^{(2)}$ in each time bin, the final step is to express this

representation in terms of spherical harmonics. The following procedure is applied on a bin-by-bin base.

In a current-free region, representing the Earth's atmosphere in the near-space environment, the magnetic field components Z and X of model MMC$^{(2)}$ can be expanded in series of complex scalar spherical harmonics in the spherical SM coordinates $Y_{jm}(\Omega_{\rm sm})$ (e.g., Varshalovich et al. 1989, Chapter 5) and their derivatives (e.g., Martinec 1999),

$$\begin{aligned} Z(r,\Omega_{\rm sm}) &= \sum_{j=1}^{j_{\max}} \sum_{m=-j}^{j} \left[j \left(\frac{r}{R_e}\right)^{j-1} G_{jm}^{(\rm e)} - (j+1) \left(\frac{R_e}{r}\right)^{j+2} G_{jm}^{(\rm i)} \right] Y_{jm}(\Omega_{\rm sm}), \\ X(r,\Omega_{\rm sm}) &= \sum_{j=1}^{j_{\max}} \sum_{m=-j}^{j} \left[\left(\frac{r}{R_e}\right)^{j-1} G_{jm}^{(\rm e)} + \left(\frac{R_e}{r}\right)^{j+2} G_{jm}^{(\rm i)} \right] \frac{\partial Y_{jm}(\cos\vartheta_{\rm sm})}{\partial \vartheta_{\rm sm}}, \end{aligned} \tag{18}$$

where $G_{jm}^{(\rm e)}$ and $G_{jm}^{(\rm i)}$ are complex spherical harmonic coefficients of the external and internal magnetic fields of model MMC$^{(2)}$, respectively; the expansions (18) are cut at degree $j_{\max}$.

In real arithmetic, the external part of Eq. (18) for fixed radius $r = R_e$ takes the form

$$\begin{aligned} Z^{(\rm e)}(\Omega_{\rm sm}) &= \sum_{j=1}^{j_{\max}} \left[j\, C_{j0}^{(\rm e)} P_{j0}(\cos\vartheta_{\rm sm}) + j \sum_{m=1}^{j} \left(C_{jm}^{(\rm e)} \cos(m\varphi_{\rm sm}) + S_{jm}^{(\rm e)} \cos(m\varphi_{\rm sm}) \right) P_{jm}(\cos\vartheta_{\rm sm}) \right], \\ X^{(\rm e)}(\Omega_{\rm sm}) &= \sum_{j=1}^{j_{\max}} \left[C_{j0}^{(\rm e)} \frac{\partial P_{j0}(\cos\vartheta_{\rm sm})}{\partial \vartheta_{\rm sm}} \right. \\ &\quad \left. + \sum_{m=1}^{j} \left(C_{jm}^{(\rm e)} \cos(m\varphi_{\rm sm}) + S_{jm}^{(\rm e)} \cos(m\varphi_{\rm sm}) \right) \frac{\partial P_{jm}(\cos\vartheta_{\rm sm})}{\partial \vartheta_{\rm sm}} \right], \end{aligned} \tag{19}$$

where $C_{jm}^{(\rm e)}$ and $S_{jm}^{(\rm e)}$ are real spherical harmonic coefficients of the external magnetic field of model MMC$^{(2)}$, and $P_{jm}(\cos\vartheta_{\rm sm})$ is the Legendre function of degree j and order m. Analogous expressions hold for the internal magnetic field components of model MMC$^{(2)}$, except the multiplicative factor j occurring in the expression for $Z^{(\rm e)}$ is to be replaced by factor $-(j+1)$ in component $Z^{(\rm i)}$. Cosine and sine coefficients $C_{jm}^{(\rm e,i)}$ and $S_{jm}^{(\rm e,i)}$ are functions of the parameters of model MMC$^{(2)}$. Because the external and internal magnetic fields of MMC$^{(2)}$ are represented separately by the external and internal electric currents, the corresponding SH coefficients can also be represented separately by either external or internal electric current parameters. For instance, the representation of the external magnetic field of model MMC$^{(2)}$ by either electric current parameters a_e, I_e and x_{0e}, or coefficients $C_{jm}^{(\rm e)}$ and $S_{jm}^{(\rm e)}$ means that the two sets of parameters are mutually related,

$$\begin{aligned} C_{jm}^{(\rm e)} &= \hat{C}_{jm}^{(\rm e)}(a_e, I_e, x_{0e}), \\ S_{jm}^{(\rm e)} &= \hat{S}_{jm}^{(\rm e)}(a_e, I_e, x_{0e}). \end{aligned} \tag{20}$$

Similarly,

$$\begin{aligned} C_{jm}^{(\rm i)} &= \hat{C}_{jm}^{(\rm i)}(a_i, I_i, x_{0i}), \\ S_{jm}^{(\rm i)} &= \hat{S}_{jm}^{(\rm i)}(a_i, I_i, x_{0i}). \end{aligned} \tag{21}$$

However, there is no analytical expression of functions $\hat{C}_{jm}^{(\rm e)}$ and $\hat{S}_{jm}^{(\rm e)}$ because they are non-linear with respect to parameters a_e and x_{0e}. The functional dependencies are thus set up numerically. We first sample the external magnetic field of MMC$^{(2)}$ in an equiangular grid on a sphere of radius R_e from the values of parameters a_e, I_e and x_{0e}, and then perform the SH analysis of the samples

(See figure on next page.)

Fig. 14 The same as Fig. 4, but for the Swarm residuals $\Delta X_{\rm sm}^{(2)}$ (thin black), $\Delta Y_{\rm sm}^{(2)}$ (thin green) and $\Delta Z^{(2)}$ (thin orange) that are corrected for the magnetic fields of PEJs and FACs and grouped in discrete time bins of 1-h duration before the adjustment by the two-circular loop model of MRCs and MICs. The resulting MMF, denoted as MMC$^{(2)}$, revises the first-order estimate of MMF, denoted as MMC$^{(1)}$, for which determination no corrections due to PEJs and FACs have been applied. Vertical dashed violet lines denote the mid-latitude interval $I_{\rm ML}^{10^\circ}$

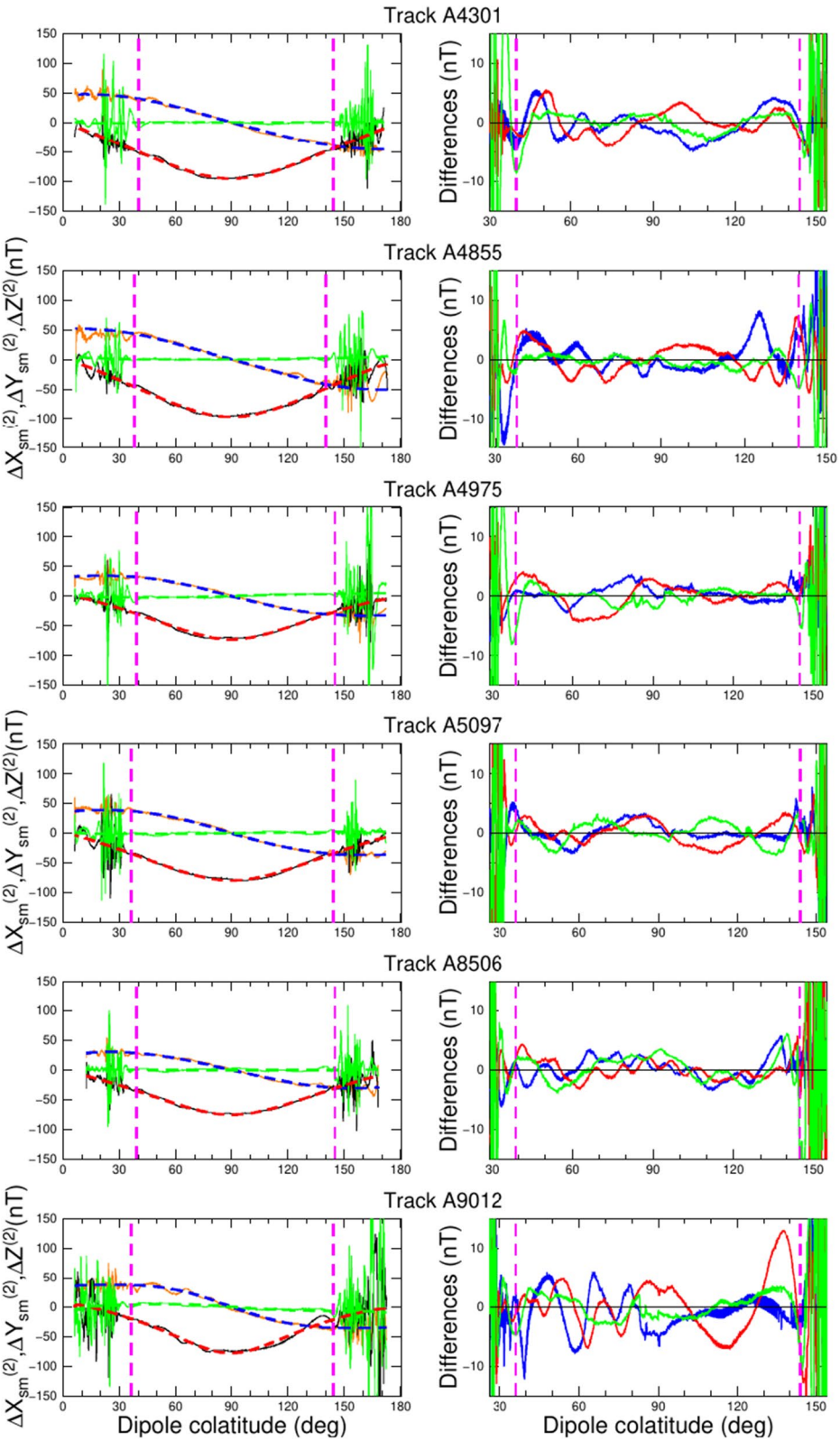

Fig. 14 (See legend on previous page.)

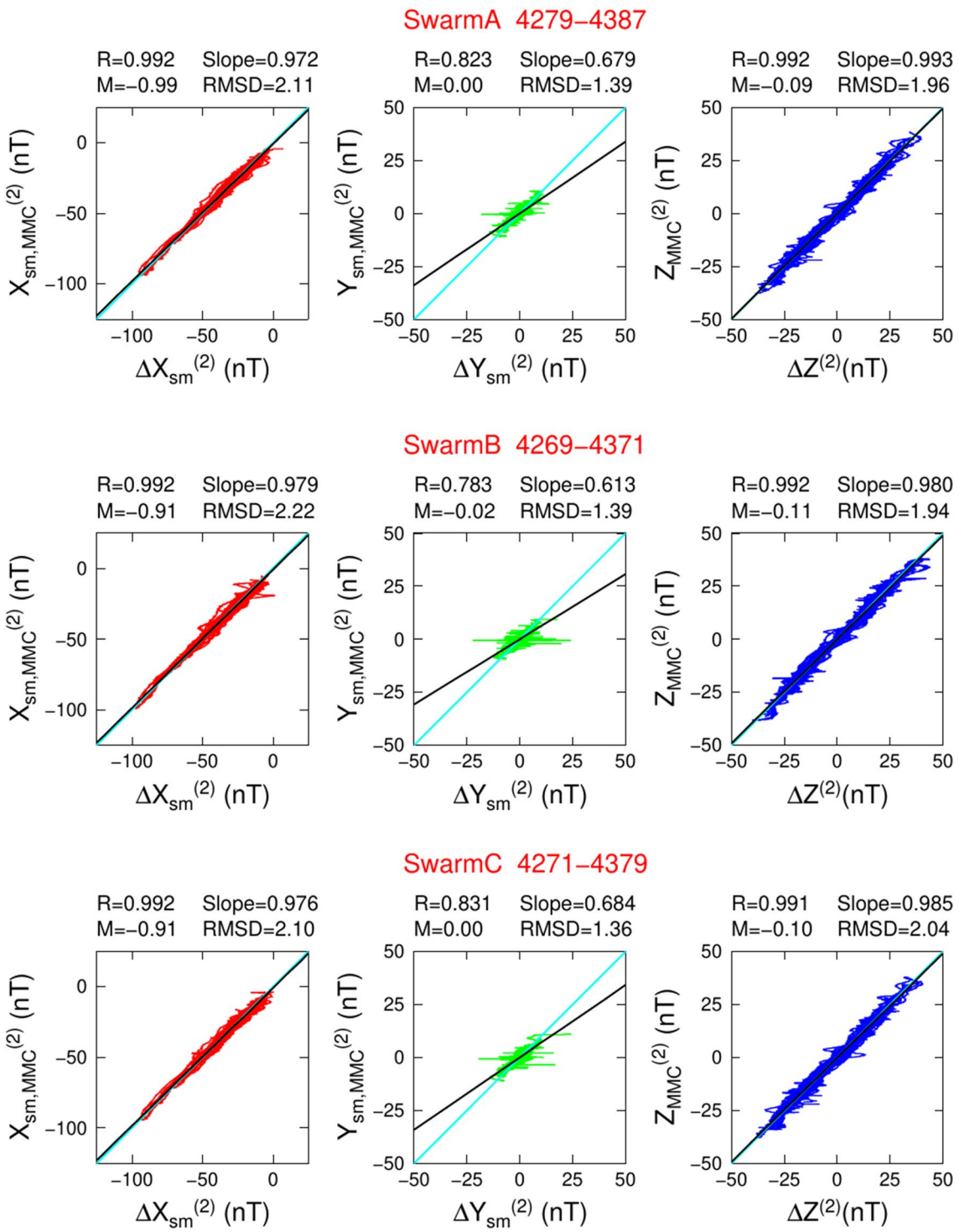

Fig. 15 The same as Fig. 5, but for the magnetic field components $X^{(2)}_{\mathrm{sm,MMC}}$, $Y^{(2)}_{\mathrm{sm,MMC}}$ and $Z^{(2)}_{\mathrm{MMC}}$ due to the two-circular loop model of MRCs and MICs. The analysis of residuals is carried out in bins of 1-h duration

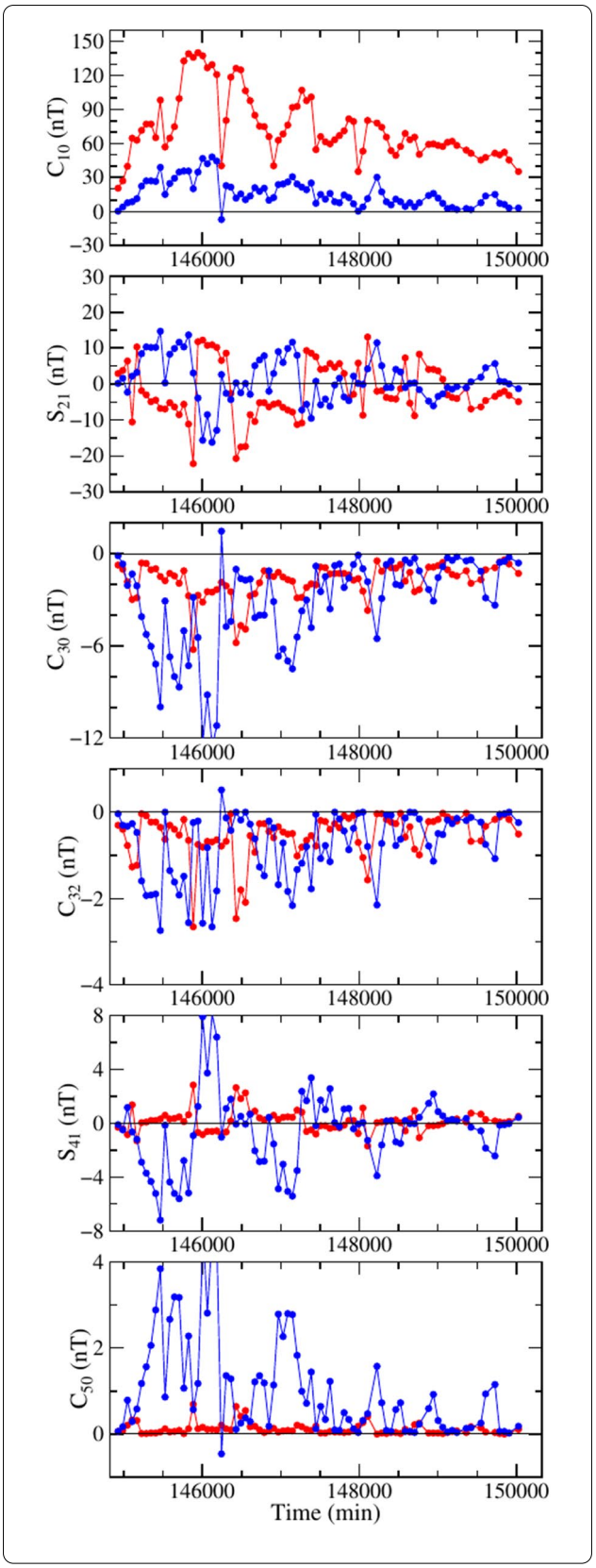

Fig. 16 The time evolution of external coefficients $C_{jm}^{(e)}$ and $S_{jm}^{(e)}$ (red), and internal coefficients $C_{jm}^{(i)}$ and $S_{jm}^{(i)}$ (blue) up to degree $j = 5$ whose magnitudes are larger than 1 nT. Time span covers the magnetic storm analysed in Fig. 1

to determine $C_{jm}^{(e)}$ and $S_{jm}^{(e)}$ coefficients (e.g., Martinec 1991; Martinec and Einšpigel 2018). An analogous procedure results in the determination of the internal magnetic field coefficients $C_{jm}^{(i)}$ and $S_{jm}^{(i)}$.

Figure 16 shows the time evolution of coefficients $C_{jm}^{(e,i)}$ and $S_{jm}^{(e,i)}$ during the magnetic storm analysed in Fig. 1. Only those coefficients whose magnitudes are larger than 1 nT are plotted. We can see that there are 5 external coefficients $C_{10}^{(e)}$, $S_{21}^{(e)}$, $C_{30}^{(e)}$, $C_{32}^{(e)}$ and $S_{41}^{(e)}$ satisfying this selection criterion. As far the internal coefficients, beside those of the same degrees and orders as the external coefficients, there are also others, higher degree coefficients $C_{50}^{(i)}$, $C_{52}^{(i)}$, $S_{61}^{(i)}$, $C_{70}^{(i)}$, $C_{72}^{(i)}$, $S_{81}^{(i)}$, and $C_{90}^{(i)}$, whose magnitudes are larger than 1 nT (not shown). A more rich spectrum of internal coefficients corresponds to the expectation (Olsen et al. 2006) because the distance between Swarm satellite orbits and the induced currents in the Earth is significantly smaller than the distance between Swarm orbits and the magnetospheric ring currents. Hence, a Swarm onboard magnetometer is more sensitive to small-scale features of the magnetic field due to induced currents in the Earth than those generated by the magnetospheric ring currents. As also expected, both degree-one and order-zero coefficients are largest in magnitudes. The external and internal order-one coefficients reflect the shift of magnetospheric ring currents and their induced counterparts in the Earth along the SM axis y_{sm} on the nightsides.

Conclusions

A way to estimate the electrical conductivity of the Earth's mantle below depths of 300–400 km is to analyse and interpret magnetic signals recorded by satellite and ground-based observatory magnetometers. We should mainly focus on large magnetic storms because the associated eddy currents induced in the Earth penetrate deep in the mantle and thus illuminate deeper parts of the Earth. The method proposed in this paper is meant to apply mainly to magnetic signals recorded by Swarm satellites during magnetic storms. The method also performs well for Swarm magnetic signals recorded at magnetically quiet times, however, those signals are not of primary interest of this paper.

There are two principal difficulties when processing Swarm magnetic signals during magnetic storms. The first concerns the magnetic fields of PEJs and FACs which are significantly enlarged during magnetic storms. They contribute by the largest signals to Swarm

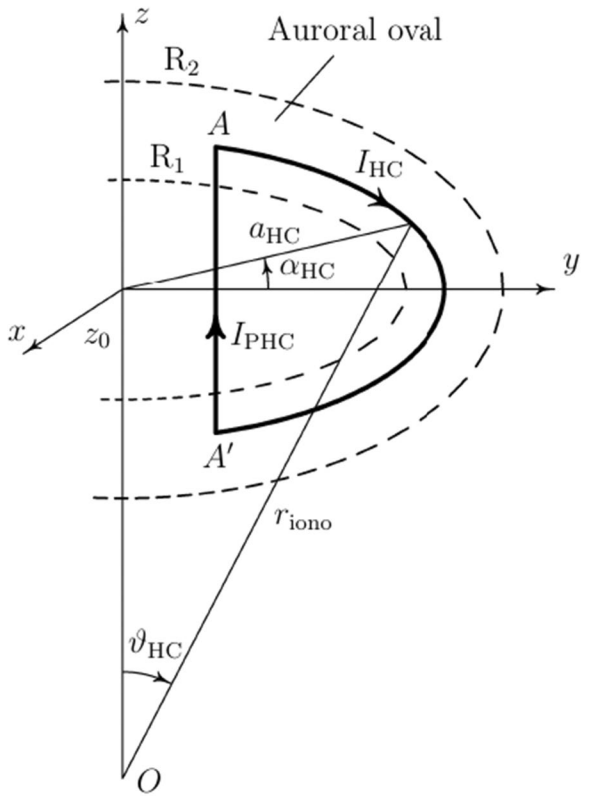

Fig. 17 The geometry considered to derive the magnetic field generated by a wire lying in the westward auroral electrojet and carrying the Hall current I_{HC} along a circular arc. The arc has the geocentric colatitude ϑ_{HC}, radius $a_{\mathrm{HC}} = r_{\mathrm{iono}} \sin \vartheta_{\mathrm{HC}}$ and is shifted along the z axis by $z_0 = r_{\mathrm{iono}} \cos \vartheta_{\mathrm{HC}}$. The arc extends from $-\alpha_{\mathrm{HC}}$ to α_{HC}, where α_{HC} is the angle counted counterclockwise from the y axis in the horizontal plain. The Hall currents I_{HC} are enclosed by the polar-cap Hall current I_{PHC} that flow sunwards across the polar cap along the circular arc $A - A'$

magnetic residuals in polar regions, but they also have a rather significant contribution to Swarm measurements in mid-latitudes. It causes a problem because the mid-latitude Swarm data are used to estimate the MMF and its induced counterpart in the Earth by the spectral methods (Sabaka et al. 2020; Martinec et al. 2018). Both spectral methods assume that the magnetic disturbing effect of PEJs and FACs on mid-latitude measurements is negligible. We have abandoned this assumption in this paper because it is violated for the X and Y (and slightly for Z) components of Swarm measurements. Instead, we have designed a complex model of electric currents in the polar ionosphere and along field lines of the main magnetic field, and used it to model the magnetic fields of PEJs and FACs along complete Swarm tracks. The model parameters of PEJ and FAC electric currents are estimated by solving a non-linear inverse problem, which is non-unique and unstable. Despite ill conditioned, the regularisation by a simple Tikhonov approach results in well-behaving magnetic fields of PEJs and FACs.

By subtracting these fields from Swarm magnetic residuals, we are in a more favourable position to search for the magnetic fields of the magnetospheric ring currents and their counterparts induced in the Earth. Here, we are faced the second difficulty of how to separate Swarm residuals into the magnetic fields of external and internal origins. In this paper, we design a complex electric current model composed of electric currents in the inner magnetosphere and the Earth that naturally separates Swarm magnetic residuals into the external and internal origins. The design of the model is simple due to two reasons. First, the MMF is quickly changing in time and space during magnetic storms while only three satellite measurements are available in discrete time bins for which a MMF may be assumed to be constant in time (but varying spatially). This restricts the complexity of MMF model. Second, the inverse problem for estimating the model parameters is non-unique. However, the combination of a grid search technique with a priori restrictions on model parameters and least-squares overcome this difficulty.

We have assessed the newly derived magnetospheric magnetic field model MMC by the scatter plots between the model and data used to construct the model. By this criterion, the new model performs significantly better than the existing magnetospheric magnetic field model MMA at magnetically disturbed times. A better performance of model MMC is explained by the fact that highly spatially and temporarily varying magnetic fields of PEJs and FACs have been modelled and subtracted from Swarm residuals prior to searching for a MMF.

The electric current parameterisation of model MMC has been transformed to a spherical harmonic parameterisation. This shows that the internal part of MMC is more rich on larger-in-amplitude spherical harmonics than the external part of model MMC, which was the expectation before launching Swarm mission.

Appendix A: Magnetic field generated by a steady current

Consider a wire carrying a steady current I along a curve (or path) C. The Biot–Savart law gives the magnetic field contribution, $d\boldsymbol{B}$, from the current source, $I d\boldsymbol{s}$, at the field point $\boldsymbol{r}$ as

$$d\boldsymbol{B}(\boldsymbol{r}) = \frac{\mu_0}{4\pi} \frac{I d\boldsymbol{s} \times \boldsymbol{d}}{d^3}, \tag{A.1}$$

where $d\boldsymbol{s}$ is an infinitesimal tangent vector to C, $\boldsymbol{d}$ is the displacement vector in the direction pointing from the wire element $d\boldsymbol{s}$ at point $\boldsymbol{r}'$ towards the point $\boldsymbol{r}$ at which the magnetic field is being calculated,

$$\boldsymbol{d} = \boldsymbol{r} - \boldsymbol{r}', \tag{A.2}$$

$d = |\vec{d}|$ and μ_0 is the vacuum permeability. The total magnetic field at $\boldsymbol{r}$ can then be obtained by integrating infinitesimal magnetic field contributions along the curve C,

$$\boldsymbol{B}(\boldsymbol{r}) = \int_C d\boldsymbol{B}(\boldsymbol{r}). \tag{A.3}$$

In this paper, we only consider electric wires represented by two-dimensional parametric curves, that is, the curves that can be placed in a plane. To parameterise PEJs and FACs, we will consider the curves lying in Cartesian coordinate surfaces and the curves lying in meridional planes.

Appendix B: A curve lying in $z = z_0$ plane

A curve lying in $z = z_0$ plane can be represented by three parametric equations:

$$\begin{aligned} x' &= R(\varphi'), \\ y' &= G(\varphi'), \\ z' &= z_0, \end{aligned} \tag{B.1}$$

where the parameter φ' is an angle, e.g., longitude or azimuth, $0 \le \varphi' < 2\pi$. Hereafter, variables with a 'prime' are used for the source point. The vector form of Eq. (B.1) is

$$\boldsymbol{r}' = R(\varphi')\boldsymbol{e}_x + G(\varphi')\boldsymbol{e}_y + z_0\boldsymbol{e}_z, \tag{B.2}$$

where $\boldsymbol{e}_x$, $\boldsymbol{e}_y$ and $\boldsymbol{e}_z$ are the Cartesian base vectors. Under the assumption that functions $R(\varphi')$ and $G(\varphi')$ are differentiable, an infinitesimal tangent vector to C is

$$d\boldsymbol{s} = \big[S(\varphi')\boldsymbol{e}_x + H(\varphi')\boldsymbol{e}_y\big]d\varphi', \tag{B.3}$$

where

$$S(\varphi') = \frac{dR(\varphi')}{d\varphi'}, H(\varphi') = \frac{dG(\varphi')}{d\varphi'}, \tag{B.4}$$

and $d\varphi'$ is an infinitesimal increment in φ'.

Representing the field point in spherical coordinates,

$$\boldsymbol{r} = r\sin\vartheta\cos\varphi\,\boldsymbol{e}_x + r\sin\vartheta\sin\varphi\,\boldsymbol{e}_y + r\cos\vartheta\,\boldsymbol{e}_z, \tag{B.5}$$

where r, ϑ and φ are radius, colatitude and longitude, respectively, the relative position vector between the source point and the field point is

$$\begin{aligned} \boldsymbol{d} = \boldsymbol{r} - \boldsymbol{r}' \;=\; & [r\sin\vartheta\cos\varphi - R(\varphi')]\boldsymbol{e}_x \\ & + [r\sin\vartheta\sin\varphi - G(\varphi')]\boldsymbol{e}_y + (r\cos\vartheta - z_0)\boldsymbol{e}_z. \end{aligned} \tag{B.6}$$

Its magnitude is

$$d = \sqrt{r^2 + R^2(\varphi') + G^2(\varphi') - 2rR(\varphi')\sin\vartheta\cos\varphi - 2rG(\varphi')\sin\vartheta\sin\varphi - 2rz_0\cos\vartheta + z_0^2}. \tag{B.7}$$

The cross product $d\boldsymbol{s} \times \boldsymbol{d}$, occurring in Eq. (A.1), is

$$\begin{aligned} d\boldsymbol{s} \times \boldsymbol{d} = \; & \big\{H(\varphi')(r\cos\vartheta - z_0)\boldsymbol{e}_x - S(\varphi')(r\cos\vartheta - z_0)\boldsymbol{e}_y \\ & + S(\varphi')[r\sin\vartheta\sin\varphi - G(\varphi')]\boldsymbol{e}_z \\ & - H(\varphi')[r\sin\vartheta\cos\varphi - R(\varphi')]\boldsymbol{e}_z\big\}d\varphi'. \end{aligned} \tag{B.8}$$

The infinitesimal contribution to the magnetic field due to $Id\boldsymbol{s}$ is given by the Biot–Savart law (A.1); its Cartesian components are:

$$\begin{aligned} dB_x &= \frac{\mu_0 I}{4\pi}\,\frac{H(\varphi')(r\cos\vartheta - z_0)}{d^3}d\varphi', \\ dB_y &= -\frac{\mu_0 I}{4\pi}\,\frac{S(\varphi')(r\cos\vartheta - z_0)}{d^3}d\varphi', \\ dB_z &= \frac{\mu_0 I}{4\pi}\,\frac{S(\varphi')[r\sin\vartheta\sin\varphi - G(\varphi')] - H(\varphi')[r\sin\vartheta\cos\varphi - R(\varphi')]}{d^3}d\varphi', \end{aligned} \tag{B.9}$$

where d is given by Eq. (B.7). Finally, substituting Eq. (B.9) into the line integral in Eq. (A.3) and integrating the result along curve C gives the total magnetic field $\boldsymbol{B}$. However, the integral is an elliptic integral that, in general, cannot be expressed in terms of elementary functions. We evaluate it by numerical quadrature.

Having computed the Cartesian component of $\boldsymbol{B}$, its spherical components are

$$\begin{pmatrix} B_r \\ B_\vartheta \\ B_\varphi \end{pmatrix} = \begin{pmatrix} \sin\vartheta\cos\varphi & \sin\vartheta\sin\varphi & \cos\vartheta \\ \cos\vartheta\cos\varphi & \cos\vartheta\sin\varphi & -\sin\vartheta \\ -\sin\varphi & \cos\varphi & 0 \end{pmatrix} \begin{pmatrix} B_x \\ B_y \\ B_z \end{pmatrix}. \tag{B.10}$$

Appendix C: A circle lying in $z = 0$ plane and shifted along the x-axis

In "Electric two-circular loop model of MRCs and MICs" section, the magnetospheric magnetic field is represented by the field of a steady current flowing along a circular loop of radius a lying on the dipole equatorial plane and shifted along the x-axis by x_0. In this case, the curve C is described by simple parametric equations

$$\begin{aligned} x' &= a\cos\varphi' + x_0, \\ y' &= a\sin\varphi', \\ z' &= 0. \end{aligned} \tag{C.1}$$

The parametric function in Eq. (B.1) are $R(\varphi') = a\cos\varphi' + x_0$ and $G(\varphi') = a\sin\varphi'$; their derivatives are $S(\varphi') = -a\sin\varphi'$ and $H(\varphi') = a\cos\varphi'$. The infinitesimal contribution to the magnetic field at point $\boldsymbol{r}$ due to an infinitesimal current element $Id\boldsymbol{s}$ is given by (B.9). The total magnetic field at point $\boldsymbol{r}$ is given by (A.3), where the line integral is carried out for $0 \le \varphi' < 2\pi$.

Appendix D: A circular arc lying in $z = z_0$ plane

In Subsection "An electric circuit model of FACs and Pedersen currents", the Hall currents inside the auroral electrojets are represented by the steady currents flowing along circular arcs lying in the plane $z = z_0$. A circular arc of radius a lying in $z = z_0$ plane is described by the parametric equations:

$$\begin{aligned} x' &= a\cos\varphi', \\ y' &= a\sin\varphi', \\ z' &= z_0. \end{aligned} \tag{D.1}$$

In this case, $R(\varphi') = a\cos\varphi'$ and $G(\varphi') = a\sin\varphi'$. The derivatives of functions R and G are $S(\varphi') = -a\sin\varphi'$ and $H(\varphi') = a\cos\varphi'$. The infinitesimal contribution to the magnetic field at point $\boldsymbol{r}$ due to an infinitesimal current element $Id\boldsymbol{s}$ is again given by (B.9. The total magnetic field at point $\boldsymbol{r}$ is given by (A.3), where the line integral is now carried out for $\varphi' \in (-\alpha_{\rm HC}, \alpha_{\rm HC})$.

Figure 17 shows the geometric variables describing a circular arc along which the Hall current flows in the westward auroral electrojet.

Appendix E: A circular arc lying in $y = y_0$ plane

The polar-cap Hall currents flowing sunwards across the polar cap will be represented by the steady currents flowing along circular arcs lying in the $y = y_0$ plane. A circular arc of radius a lying in the $y = y_0$ plane is represented by the parametric equations:

$$\begin{aligned} x' &= R(\varphi'), \\ y' &= y_0, \\ z' &= G(\varphi'), \end{aligned} \tag{E.1}$$

where $R(\varphi') = a\sin\varphi'$ and $G(\varphi') = a\cos\varphi'$; their derivatives are $S(\varphi') = dR(\varphi')/d\varphi' = a\cos\varphi'$ and $H(\varphi') = dG(\varphi')/d\varphi' = -a\sin\varphi'$. In a similar way to Subsection A1, it can be shown that the Biot–Savart law for an infinitesimal contribution to the magnetic field due to $Id\boldsymbol{s}$ is

$$\begin{aligned} dB_x &= -\frac{\mu_0 I}{4\pi}\,\frac{H(\varphi')(r\sin\vartheta\sin\varphi - y_0)}{d^3}d\varphi', \\ dB_y &= -\frac{\mu_0 I}{4\pi}\,\frac{S(\varphi')[r\cos\vartheta - G(\varphi')] - H(\varphi')[r\sin\vartheta\cos\varphi - R(\varphi')]}{d^3}d\varphi', \\ dB_z &= \frac{\mu_0 I}{4\pi}\,\frac{S(\varphi')(r\sin\vartheta\sin\varphi - y_0)}{d^3}d\varphi', \end{aligned} \tag{E.2}$$

where d is

$$d = \sqrt{r^2 + R^2(\varphi') + G^2(\varphi') - 2rR(\varphi')\sin\vartheta\cos\varphi - 2rG(\varphi')\cos\vartheta - 2ry_0\sin\vartheta\sin\varphi + y_0^2}. \tag{E.3}$$

The total magnetic field at point $\boldsymbol{r}$ is given by (A.3), where the line integral is now carried out for $\varphi' \in (-\beta_A, \beta_A)$.

To derive an expression for β_A, Fig. 18 shows a circular arc extending between point A and A' along which the polar-cap Hall current flows in the northern polar ionosphere. Figure 17 shows that the radius of point A in the horizontal xy plane is

$$a_A = r_{\rm iono}\sin\vartheta_A, \tag{E.4}$$

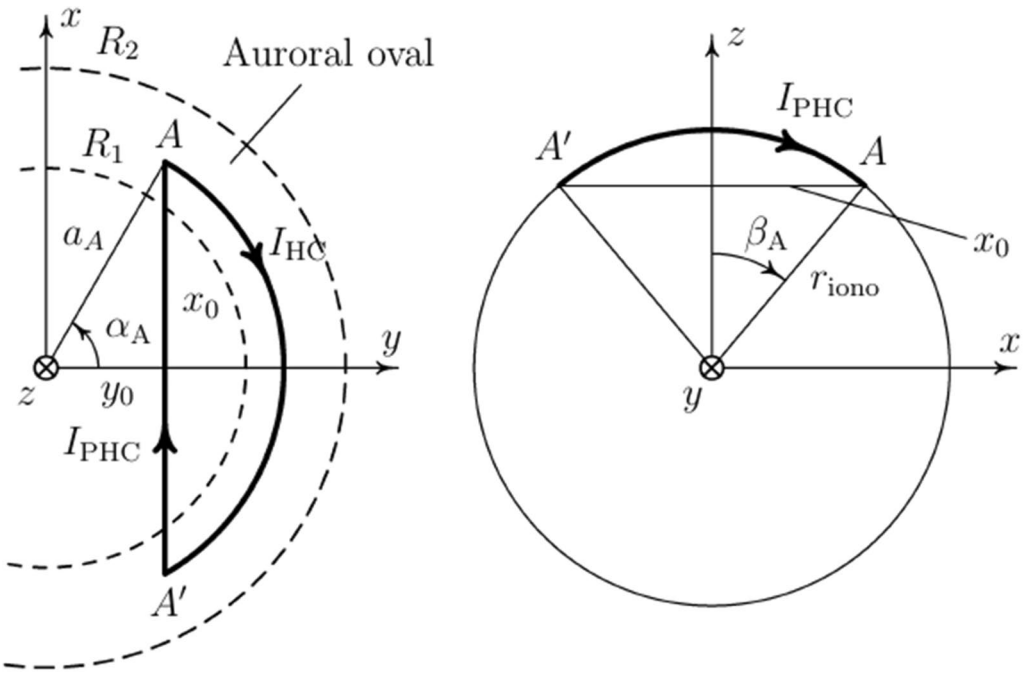

Fig. 18 The geometry considered to derive the magnetic field generated by a wire lying in $y = y_0$ plane and carrying the polar-cap Hall current $I_{\rm PHC}$ along a circular arc between points A and A'. The left and right panels show the projections onto the $z = z_0$ and $y = y_0$ planes, respectively, where $z_0 = r_{\rm iono}\cos\vartheta_A$, $a_A = r_{\rm iono}\sin\vartheta_A$ (see Fig. 17) and $y_0 = a_A\cos\alpha_A$

where ϑ_A is the colatitude of point A. Its projections onto the x and y axes are

$$\begin{aligned} x_0 &= a_A \sin\alpha_A, \\ y_0 &= a_A \cos\alpha_A, \end{aligned} \tag{E.5}$$

respectively, where the azimuth α_A of point A is measured counterclockwise from the y axis. The circular arc A–A' with the polar-cap Hall current lies in the $y = y_0$ plane and has radius $r_{\rm iono}$; it extends from $-\beta_A$ to β_A. The right panel of Fig. 18 shows that

$$\sin\beta_A = \frac{x_0}{r_{\rm iono}}, \tag{E.6}$$

or,

$$\sin\beta_A = \sin\vartheta_A \sin\alpha_A. \tag{E.7}$$

Appendix F: A circular arc lying in $x = x_0$ plane

The polar-cap Pedersen currents flowing eastwards or westwards across the polar cap will be represented by the steady currents flowing along circular arcs lying in the $x = x_0$ plane. A circular arc of radius a lying in the $x = x_0$ plane is represented by the parametric equations:

$$\begin{aligned} x' &= x_0, \\ y' &= R(\varphi'), \\ z' &= G(\varphi'), \end{aligned} \tag{F.1}$$

where $R(\varphi') = a\cos\varphi'$ and $G(\varphi') = a\sin\varphi'$; their derivatives are $S(\varphi') = dR(\varphi')/d\varphi' = -a\sin\varphi'$ and $H(\varphi') = dG(\varphi')/d\varphi' = a\cos\varphi'$. In a similar way to Subsection A1, it can be shown that the Biot–Savart law for an infinitesimal contribution to the magnetic field due to $Id\boldsymbol{s}$ is

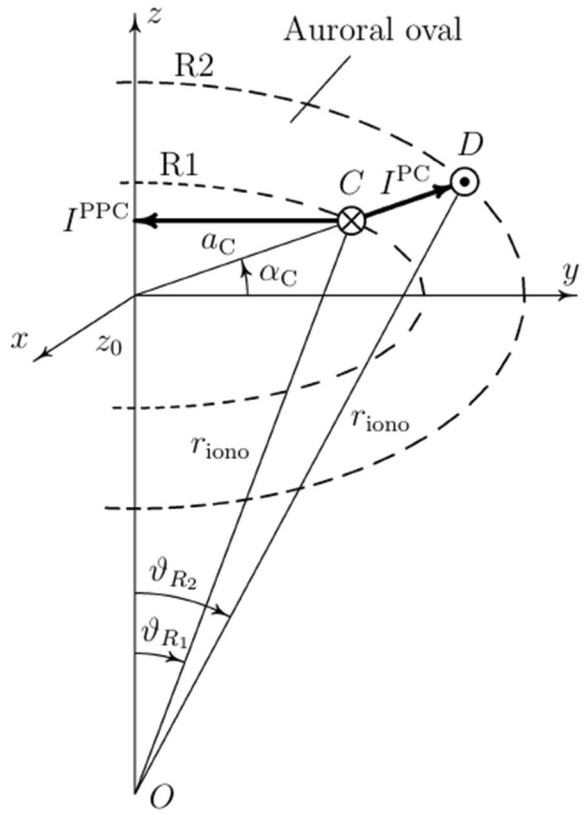

Fig. 19 The geometry considered to derive the magnetic field generated by a wire lying in the meridional plane $\varphi = \alpha_C$ and carrying the Pedersen current I_{PC} in the auroral oval along a circular arc between points C and D at Region 1 and Region 2, respectively. The arc has radius r_{iono} and extends between the geocentric colatitudes ϑ_{R_1} and ϑ_{R_2}. The polar-cap Pedersen current I_{PPC} flows across the polar cap to the opposite local-time sector. Crossed and dotted circles represent the flow of FACs into and out of the ionosphere, respectively

The total magnetic field at point $\boldsymbol{r}$ is given by (A.3), where the line integral is now carried out for $\varphi' \in (-\gamma_C, \gamma_C)$.

To derive an expression for γ_C, the left panel of Fig. 20 shows a circular arc extending between point C and C' along which the polar-cap Pedersen current crosses the polar-cap ionosphere. Figure 19 shows that the radius of point C in the horizontal xy plane is

$$a_C = r_{\rm iono} \sin \vartheta_{R_1}. \tag{F.4}$$

Its projections onto the x and y axes are

$$\begin{aligned} x_0 &= a_C \sin \alpha_C, \\ y_0 &= a_C \cos \alpha_C, \end{aligned} \tag{F.5}$$

respectively, where α_C is the azimuth of point C. The arc C–C' with the polar-cap Pedersen current lies in $x = x_0$ plane and has radius $r_{\rm iono}$; it extends from $-\gamma_C$ to γ_C. The second panel of Fig. 20 shows that

$$\sin \gamma_C = \frac{y_0}{r_{\rm iono}}, \tag{F.6}$$

or,

$$\sin \gamma_C = \sin \vartheta_{R_1} \cos \alpha_C. \tag{F.7}$$

Appendix G: A curve in a meridional plane

In Subsection "An electric circuit model of Hall currents", the Pedersen currents in the auroral ovals and the field-aligned currents are represented by the steady currents flowing along curves lying in the xz plane that is rotated along the z axis by angle α, that is, in the meridional plane $\varphi = \alpha$.

To find the form of the Biot–Savart law in this case, let us first rotate the xz plane (i.e., the $y = 0$ plane, or the zero-degree meridian plane) around the z axis by angle α

$$\begin{aligned} dB_x &= \frac{\mu_0 I}{4\pi} \frac{S(\varphi')[r\cos\vartheta - G(\varphi')] - H(\varphi')[r\sin\vartheta\sin\varphi - R(\varphi')]}{d^3} d\varphi', \\ dB_y &= \frac{\mu_0 I}{4\pi} \frac{H(\varphi')(r\sin\vartheta\cos\varphi - x_0)}{d^3} d\varphi', \\ dB_z &= -\frac{\mu_0 I}{4\pi} \frac{S(\varphi')(r\sin\vartheta\cos\varphi - x_0)}{d^3} d\varphi', \end{aligned} \tag{F.2}$$

where d is

$$d = \sqrt{r^2 + R^2(\varphi') + G^2(\varphi') - 2rR(\varphi')\sin\vartheta\sin\varphi - 2rG(\varphi')\cos\vartheta - 2rx_0\sin\vartheta\cos\varphi + x_0^2}. \tag{F.3}$$

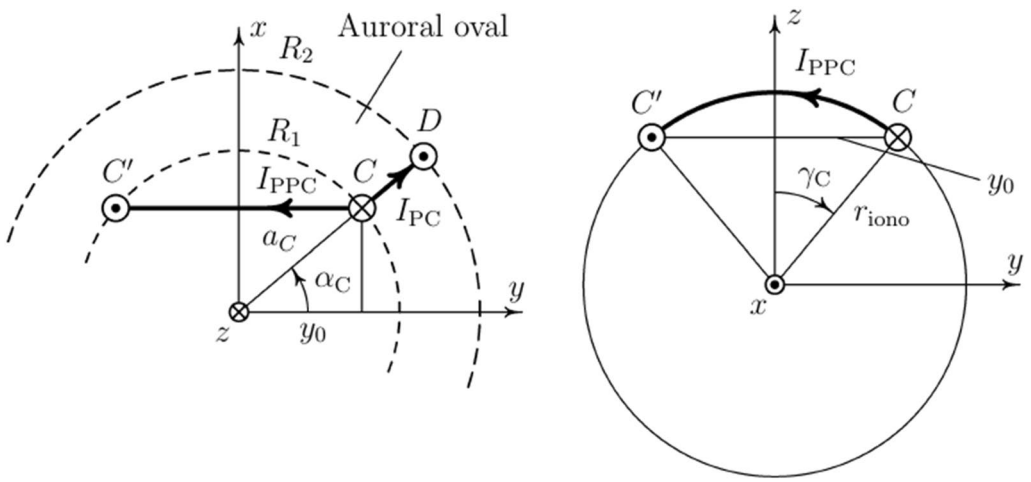

Fig. 20 The geometry considered to derive the magnetic field generated by a wire lying in $x = x_0$ plane and carrying the polar-cap Pedersen current $I_{\rm PPC}$ along a circular arc between points C and C'. The left and right panels show the projections onto the $z = z_0$ and $x = x_0$ planes, respectively, where $z_0 = r_{\rm iono}\cos\vartheta_{R_1}$, $a_C = r_{\rm iono}\sin\vartheta_{R_1}$ (see Fig. 19) and $x_0 = a_C\sin\alpha_C$. Large crossed and dotted circles represent the flow of FACs into and out of the ionosphere, respectively

and place curve C in the rotated $x_{\rm rot}z$ plane (label 'rot' at x stands for 'rotated'). The parametric equations of C in the rotated $x_{\rm rot}z$ plane are

$$\begin{aligned} x'_{\rm rot} &= R(\vartheta'),\\ y'_{\rm rot} &= 0,\\ z' &= G(\vartheta'). \end{aligned} \tag{G.1}$$

We choose the colatitude for the parameter ϑ' of curve C. The position vector of a (source) point lying on the curve C in the rotated $x_{\rm rot}z$ plane is

$$\boldsymbol{r}'_{\rm rot} = R(\vartheta')\boldsymbol{e}_{x,\rm rot} + G(\vartheta')\boldsymbol{e}_z, \tag{G.2}$$

where the Cartesian base vector $\boldsymbol{e}_{x,\rm rot}$ in the rotated $x_{\rm rot}z$ plane can be expressed in terms of the Cartesian base vector in the (non-rotated) xz plane as

$$\boldsymbol{e}_{x,\rm rot} = \cos\alpha\,\boldsymbol{e}_x + \sin\alpha\,\boldsymbol{e}_y. \tag{G.3}$$

Hence, the position vector of a point on curve C expressed in terms of the (non-rotated) Cartesian base vectors is

$$\boldsymbol{r}' = R(\vartheta')(\cos\alpha\,\boldsymbol{e}_x + \sin\alpha\,\boldsymbol{e}_y) + G(\vartheta')\boldsymbol{e}_z. \tag{G.4}$$

An infinitesimal tangent vector to C is

$$d\boldsymbol{s} = \big[S(\vartheta')(\cos\alpha\,\boldsymbol{e}_x + \sin\alpha\,\boldsymbol{e}_y) + H(\vartheta')\boldsymbol{e}_z\big]d\vartheta'. \tag{G.5}$$

Substituting the last two equations and Eq. (B.5) into Eq. (A.1), the Biot–Savart law for an infinitesimal contribution to the magnetic field due to $Id\boldsymbol{s}$ is

$$\begin{aligned} dB_x &= \frac{\mu_0 I}{4\pi}\,\frac{\sin\alpha\,S(\vartheta')[r\cos\vartheta - G(\vartheta')] - H(\vartheta')[r\sin\vartheta\cos\varphi - \sin\alpha\,R(\vartheta')]}{d^3}d\vartheta',\\ dB_y &= -\frac{\mu_0 I}{4\pi}\,\frac{\cos\alpha\,S(\vartheta')[r\cos\vartheta - G(\vartheta')] - H(\vartheta')[r\sin\vartheta\cos\varphi - \cos\alpha\,R(\vartheta')]}{d^3}d\vartheta',\\ dB_z &= \frac{\mu_0 I}{4\pi}\,\frac{\cos\alpha\,S(\vartheta')r\sin\vartheta\sin\varphi - \sin\alpha\,S(\vartheta')r\sin\vartheta\cos\varphi}{d^3}d\vartheta', \end{aligned} \tag{G.6}$$

where d is

$$d = \sqrt{r^2 + R^2(\vartheta') + G^2(\vartheta') - 2rR(\vartheta')\sin\vartheta\cos\varphi\cos\alpha - 2rR(\vartheta')\sin\vartheta\sin\varphi\sin\alpha - 2rG(\vartheta')\cos\vartheta}. \tag{G.7}$$

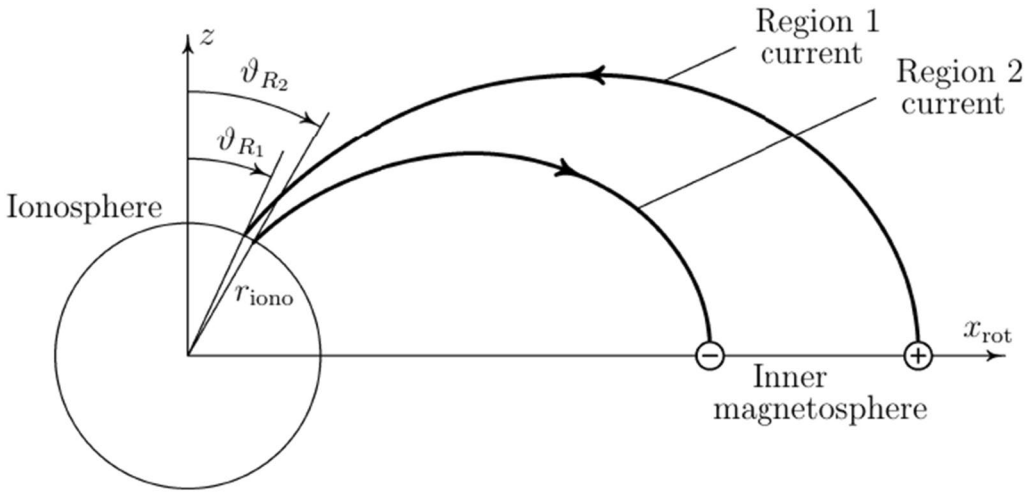

Fig. 21 The geometry considered to derive the magnetic field generated by Region 1 and Region 2 field-aligned currents connecting the northern polar ionosphere and the inner magnetosphere. The currents flow in the meridional plane $\varphi = \alpha$. The poleward Region 1 and equatorward Region 2 have colatitudes ϑ_{R_1} and ϑ_{R_2}, respectively. The electric circuit model designed in this paper considers also the second pair of Region 1 and Region 2 field-aligned currents connecting the southern polar ionosphere and the inner magnetosphere (not shown in the figure)

Appendix H: Magnetic field generated by the Pedersen current

In Subsection "An electric circuit model of FACs and Pedersen currents", the Pedersen currents inside the auroral electrojets are represented by the steady currents flowing in the meridional plane $\varphi = \alpha$ along a circular arc of radius r_{iono} between the upward and downward FACs, that is, between Region 1 and Region 2. The parametric equations of a circular arc of radius a lying in the $x_{\text{rot}}z$ plane that is rotated around the z axis by α are

$$\begin{aligned} x_{\text{rot}} &= a \sin\vartheta', \\ z &= a \cos\vartheta'. \end{aligned} \tag{H.1}$$

To follow the notation introduced in Eq. (E.1), we denote

$$\begin{aligned} R(\vartheta') &:= a \sin\vartheta', \\ G(\vartheta') &:= a \cos\vartheta'. \end{aligned} \tag{H.2}$$

The derivatives of functions R and G with respect to ϑ' are

$$\begin{aligned} S(\vartheta') &= a \cos\vartheta', \\ H(\vartheta') &= -a \sin\vartheta'. \end{aligned} \tag{H.3}$$

Substituting eqs (H.2) and (H.3) into Eq. (G.6) gives the infinitesimal contribution to the magnetic field due to current I flowing along a circular arc. The total magnetic field at point $\boldsymbol{r}$ is given by (A.3), where the line integral is now carried out for $\vartheta' \in (\vartheta_{R_1}, \vartheta_{R_2})$.

Figure 19 shows the geometric variables describing a circular arc between Region 1 and Region 2 along which the Pedersen current flows in the westward auroral electrojet.

Appendix I: Magnetic field generated by a FAC

Up to geocentric distances of approximately $8R_e$, we may assume that the electric currents between the polar ionospheres and magnetosphere flow along the Earth's magnetic dipole field lines (e.g., Tsyganenko 2013).

A field line of a magnetic dipole is given by a nonparametric equation (e.g., Baumjohann and Treumann 1996):

$$r = L_R \sin^2\vartheta, \tag{I.1}$$

where (r, ϑ) are geocentric coordinates of a point lying on a dipole field line and L_R is the distance at which the field line passing through a particular point (r_R, ϑ_R) crosses the equator (label 'R' stands for 'Region', e.g., Region 1 and Region 2 in the polar ionosphere). Consider a dipole field line lying in the meridional plane $\varphi = \alpha$ and rotate this plane around the z axis by angle α. The Cartesian components of a point lying in the $x_{\text{rot}}z$ rotated plane are

$$\begin{aligned} x_{\text{rot}} &= r \sin\vartheta, \\ z &= r \cos\vartheta. \end{aligned} \tag{I.2}$$

Substituting for r from Eq. (I.1) yields the parametric equations of a dipole field line in the rotated $x_{\text{rot}}z$ plane,

$$\begin{aligned} x_{\text{rot}} &= L_R \sin^3\vartheta, \\ z &= L_R \sin^2\vartheta \cos\vartheta. \end{aligned} \tag{I.3}$$

To follow the notation introduced in Eq. (E.1), we denote

$$\begin{aligned} R(\vartheta') &:= L_R \sin^3 \vartheta', \\ G(\vartheta') &:= L_R \sin^2 \vartheta' \cos \vartheta', \end{aligned} \tag{I.4}$$

where variables with a 'prime' are again used for source points. The derivatives of functions R and G with respect to ϑ' are

$$\begin{aligned} S(\vartheta') &= 3L_R \sin^2 \vartheta' \cos \vartheta', \\ H(\vartheta') &= L_R \sin \vartheta' (2\cos^2 \vartheta' - \sin^2 \vartheta'). \end{aligned} \tag{I.5}$$

Substituting eqs (I.4) and (I.5) into Eq. (G.6) gives the infinitesimal contribution to the magnetic field due to current I flowing along a field line of the Earth's magnetic dipole.

Figure 21 shows the paired down and up field-aligned currents connecting the magnetosphere with the high-latitude northern ionosphere via two regions, the so-called Region 1 and 2. Let the colatitude of these regions be ϑ_{R_1} and ϑ_{R_2}, respectively. Knowing ϑ_{R_i}, the parameter L_{R_i} in Eq. (I.1) for the FAC leaving or entering Region i, $i = 1, 2$, may be defined in terms of ϑ_{R_i} as:

$$L_{R_i} = \frac{r_{\text{iono}}}{\sin^2 \vartheta_{R_i}}. \tag{I.6}$$

The total magnetic field at point $\boldsymbol{r}$ is given by (A.3), where the line integral is now carried out for $\vartheta' \in (\vartheta_{R_i}, 90°)$.

Abbreviations

AEJ:: Auroral electrojet; FAC:: Field-aligned current; MIC:: Magnetospherically induced current in the Earth; MMA:: Model of MMF by Sabaka et al. (2020); MMC:: Model of MMF derived in this paper; MME:: Model of MMF by Martinec et al. (2018); MMF:: Magnetospheric magnetic field; MRC:: Magnetospheric ring current; PEJ:: Polar electrojet; R1, R2:: Region 1 and Region 2 in the polar ionosphere; RMSD:: Root-mean square of difference; SH:: Spherical harmonic; SM:: Solar magnetic.

Acknowledgements

The authors would like to thank Ciaran D. Beggan for providing us the report on results of the method by Martinec et al. (2018).

Author contributions

ZM is the author of the forward and inversion modelling software, and is responsible for all calculations and writing the manuscript. JV has downloaded and prepared input data.

Funding

This work has been done in the framework of the project 'Three-dimensional electrical conductivity in the Earth's mantle recovered from geomagnetic variations of magnetospheric, ionospheric, and tidal origin' supported by the Grant Agency of the Czech Republic through grant No. 20-07378S.

Availability of data and materials

The input data used this study are available from the webserver of the European Space Agency https://swarm-diss.eo.esa.int/. The model of MMF derived in this paper is available upon request to the corresponding author.

Declarations

Competing interests

There are no competing interests.

Author details

[1]Dublin Institute for Advanced Studies, 5 Merrion Square, Dublin 2, Ireland. [2]Department of Geophysics, Faculty of Mathematics and Physics, Charles University, V Holešovičkách 2, 180 00 Prague 8, Czech Republic.

Received: 1 June 2022 Accepted: 30 September 2022
Published online: 23 October 2022

References

Aakjær CD, Olsen N, Finlay CC (2016) Determining polar ionospheric electrojet currents from Swarm satellite constellation magnetic data. Earth Planets Space 68:140

Amm O (1997) Ionospheric elementary current systems in spherical coordinates and their application. J Geomagn Geoelectr 49:947–955

Austin PC, Steyerberg EW (2015) The number of subjects per variable required in linear regression analyses. J Clin Epidemiol 68:627–636

Banks RJ (1969) Geomagnetic variations and the electrical conductivity of the upper mantle. Geophys J Royal Astr Soc 17:457–487

Baumjohann W, Treumann RA (1996) Basic space plasma physics. Imperial College Press, London

Chen MW (2020) Chapter 5: ring current development. In: Jordanova VK, Ilie R, Chen MW (eds) Ring current investigations. Elsevier, pp 153–180

Daglis IA, Thorne RM, Baumjohann W, Orsi S (1999) The terrestrial ring current: Origin, formation, and decay. Rev Geophys 37:407–438

Finlay CC, Kloss C, Olsen N, Hammer MD, Tøffner-Clausen L, Grayver A, Kuvshinov A (2020) The CHAOS-7 geomagnetic field model and observed changes in the South Atlantic Anomaly. Earth Planets Space 72:156

Forsyth C, Shortt M, Coxon JC, Rae IJ, Freeman MP, Kalmoni NME, Jackman CM, Anderson BJ, Milan SE, Burrell AG (2018) Seasonal and temporal variations of field-aligned currents and ground magnetic deflections during substorms. J Geophys Res Space Phys 123(4):2696–2713

Friis-Christensen E, Lühr H, Hulot G (2006) Swarm: a constellation to study the Earth's magnetic field. Earth Planets Space 58:351–358

Fukushima N (1976) Generalized theorem for no ground magnetic effect of vertical currents connected with Pedersen currents in the uniform-conductivity ionosphere. Rep Ionos Space Res Jpn 30:35–40

Ganushkina YN, Liemohn MW, Dubyagin S (2018) Current systems in the Earth's magnetosphere. Rev Geophys 56:309–332

Grayver AV, Munch FD, Kuvshinov AV, Khan A, Sabaka TJ (2017) Joint inversion of satellite-detected tidal and magnetospheric signals constrains electrical conductivity and water content of the upper mantle and transition zone. Geophys Res Lett 44:6074–6081

Hansen PC (1992) Analysis of discrete ill-posed problems by means of the L-curve. SIAM Rev 34:561–580

Iijima T, Potemra TA (1976) The amplitude distribution of the field-aligned currents at northern high latitudes observed by TRIAD. J Geophys Res 81:2165–2174

Iijima T, Potemra TA, Zanetti LJ, Bythrow PF (1984) Large-scale Birkeland currents in the dayside polar region during strongly northward IMF: a new Birkeland current system. J. Geophys. Res. Space Phys 89:7441–7452

Johnsen MG (2013) Real-time determination and monitoring of the auroral electrojet boundaries. J Space Weather Space Clim 3:A28

Juusola L, Amm O, Viljanen A (2006) One-dimensional spherical elementary current systems and their use for determining ionospheric currents from satellite measurements. Earth Planets Space 58:667–678

Kamide Y (1982) The relationship between field-aligned currents and the auroral electrojets: a review. Space Sci Rev 31:127–243

Koch K-R (1999) Parameter estimation and hypothesis testing in linear models. Springer, Berlin

Laundal KM, Richmond AD (2017) Magnetic coordinate systems. Space Sci Rev 206:27–59

Liou K, Sotirelis T, Mitchell EJ (2018) North-south asymmetry in the geographic location of auroral substorms correlated with ionospheric effects. Sci Rep 8:17230
Martinec Z (1991) Program to calculate the least-squares estimates of the spherical harmonic expansion coefficients of an equally angular-gridded scalar field. Comp Phys Commun 64:140–148
Martinec Z (1999) Spectral-finite element approach to three-dimensional electromagnetic induction in a spherical earth. Geophys J Int 136:229–250
Martinec Z, Einšpigel D (2018) SHAVEL: a program for the spherical harmonic analysis of a horizontal vector field sampled in an equiangular grid on a sphere. Comp Phys Commun 233:206–214
Martinec Z, Everett ME, Velímský J (2003) Time-domain, spectral finite-element approach to transient 2-D geomagnetic induction in a spherical heterogeneous earth. Geophys J Int 155:33–43
Martinec Z, Velímský J, Haagmans R, Šachl L (2018) A two-step along-track spectral analysis for estimating the magnetic signals of magnetospheric ring current from Swarm data. Geophys J Int 212:1201–1217
McHenry MA, Clauer CR (1987) Modeled ground magnetic signatures of flux transfer events. J Geophys Res Space Phys 92:11231–11240
Menke W (2012) Geophysical data analysis: discrete inverse theory, 3rd edn. MATLAB, Elsevier, Amsterdam
Milan SE, Lester M, Cowley SWH, Brittnacher MM (2000) Dayside convection and auroral morphology during an interval of northward interplanetary magnetic field. Ann Geophys 18:436–444
Milan SE, Clausen LBN, Coxon JC, Carter JA, Walach MT, Laundal K, Østgaard N, Tenfjord P, Reistad J, Snekvik K, Korth H, Anderson BJ (2017) Overview of solar wind-magnetosphere-ionosphere-atmosphere coupling and the generation of magnetospheric currents. Space Sci Rev 206:547–573
Moretto T, Olsen N, Ritter P, Lu G (2002) Investigating the auroral electrojets with low altitude polar orbiting satellites. Ann Geophys 20:1049–1061
Olsen N (1996) A new tool for determining ionospheric currents from magnetic satellite data. Geophys Res Lett 23:3635–3638
Olsen N, Moretto T, Friis-Christensen E (2002) New approaches to explore the Earth's magnetic field. J Geodyn 33:29–41
Olsen N, Haagmans R, Sabaka TJ, Kuvshinov A, Maus S, Purucker ME, Rother M, Lesur V, Mandea M (2006) The swarm End-to-End mission simulator study: a demonstration of separating the various contributions to Earth's magnetic field using synthetic data. Earth Planets Space 58:359–370
Olsen N, Friis-Christensen E, Floberghagen R, Alken P, Beggan CD, Chulliat A, Doornbos E, da Encarnação JT, Hamilton B, Hulot G, van den IJssel J, Kuvshinov A, Lesur V, Lühr H, Macmillan S, Maus S, Noja M, Olsen PEH, Park J, Plank G, Püthe C, Rauberg J, Ritter P, Rother M, Sabaka TJ, Schachtschneider R, Sirol O, Stolle C, Thébault E, Thomson AWP, Tøffner-Clausen L, Velímský J, Vigneron P, Visser PN, (2013) The Swarm satellite constellation application and research facility (SCARF) and Swarm data products. Earth Planets Space 65(11):1189–1200
Onovughe E (2018) Usage of RC index as a good representation for characterising rapid variation signals in geomagnetic field studies. Sun Geosphere 13(1):77–87
Popov VA, Papitashvili VO, Watermann JF (2001) Modeling of equivalent ionospheric currents from meridian magnetometer chain data. Earth Planets Space 53:129–137
Potemra TA (1983) Magnetospheric currents. Johns Hopkins Univ APL Tech Digest 4:276–284
Prokhorov BE, Förster M, Lesur V, Namgaladze AA, Holschneider M, Stolle C (2018) Modeling of the ionospheric current system and calculating its contribution to the Earth's magnetic field. In: Lühr H, Wicht J, Gilder SA, Holschneider M (eds) Magnetic fields in the solar system: planets, moons and solar wind interactions, chapter 10. Springer, pp 263–292
Püthe C, Kuvshinov A, Khan A, Olsen N (2015) A new model of earth's radial conductivity structure derived from over 10 yr of satellite and observatory magnetic data. Geophys J Int 203(3):1864. https://doi.org/10.1093/gji/ggv407
Ritter P, Viljanen A, Lühr H, Amm O, Olsen N (2003) Ionospheric currents from CHAMP magnetic field data comparison with ground based measure ments. In: Reigber C, Lühr H, Schwintzer P (eds) First CHAMP mission results for gravity. Magnetic and atmospheric studies. Springer, Berlin, pp 347–352
Sabaka TJ, Tøffner-Clausen L, Olsen N, Finlay CC (2018) A comprehensive model of Earth's magnetic field determined from 4 years of Swarm satellite observations. Earth Planets Space 70:130
Sabaka TJ, Tøffner-Clausen L, Olsen N, Finlay CC (2020) CM6: a comprehensive geomagnetic field model derived from both CHAMP and Swarm satellite observations. Earth Planets Space 72:80
Shore R, Whaler K, Macmillan S, Beggan C, Velímský J, Olsen N (2016) Decadal period external magnetic field variations determined via eigenanalysis. J Geophys Res Space Phys 121:5172–5184
Tikhonov AN (1963) Solution of incorrectly formulated problems and the regularization method. Dokl Akad Nauk SSSR 151:501–504
Tsyganenko NA (2013) Data-based modelling of the Earth's dynamic magnetosphere: a review. Ann Geophys 31:1745–1772
Varshalovich DA, Moskalev AN, Khersonskii VK (1989) Quantum theory of angular momentum. World Scientific Publ, Singapore
Vasyliūnas VM (1999) A note on current closure. J Geophys Res Space Phys 104:25,143-25,144
Velímský J, Martinec Z (2005) Time-domain, spherical harmonic-finite element approach to transient three-dimensional geomagnetic induction in a spherical heterogeneous earth. Geophys J Int 161:81–101

Publisher's Note